TÉCNICO LISBOA

Finite Element Modelling of Damage and Failure in Fiber Reinforced Composites

Alvaro Díaz Sáez

Thesis to obtain the Master of Science Degree in

Aerospace Engineering

Supervisors: Prof. Nuno Miguel Rosa Pereira Silvestre

Eng. António Pedro Carones Duarte

Examination Committee

Chairperson: Prof. Filipe Szolnoky Ramos Pinto Cunha

Supervisor: Prof. Nuno Miguel Rosa Pereira Silvestre

Members of the Committee: Prof. Aurélio Lima Araújo

May 2015

To my family

“Nothing is lost while there

is hope for finding it”

Acknowledgments

This thesis is the result of the work done during the 7 months of my Erasmus stay in the UL (Universidade de Lisboa) at IST (Instituto Superior Técnico), which is one of the institutions with more reputation in the engineering field in Portugal. During this period, I have really enriched myself culturally as well as intellectually and personally.

Firstly, I would like to thank the support and dedication of my supervisor, the Professor Nuno Silvestre, who has guided me through their knowledge in order to develop this thesis. Thanks are also extended to my co-supervisor, Eng. Antonio Duarte for his constant assistance and help in many computational issues.

To all my Friends, for their constant support during these last years of my degree and for making me smile in the hardest moments. With special mention to Aurelio, for its help and friendship during my stay at the university.

To all my Erasmus mates, who started being strangers and turned into friends. Thank you for making me feel like at home.

Finally, thank to my family, whose support and confidence have been a motivation. Especially to my parents and my sister who, with their work and their daily struggle, will always be a model for me. Thank you. Gracias! Obrigado!

Abstract

Modelling of the damage and failure in fiber reinforced composites through the use of finite element method is the main objective of this dissertation. During the service life of the aircraft, cracks and damages may appear and develop in aeronautical structures, which should be analyzed to determine the decrease of stiffness and resistance due to the presence of the cracks.

First, a literature review on the subject is done, describing different studies in this field as well as the existing methods that can be used to predict the onset and growth of cracks and damage. Through this work, the behavior of different composite plates with holes are analyzed with Hashin-based damage method and XFEM (eXtended Finite Element Method). The models are validated by comparison with experimental results available in the literature and the computational results obtained with Abaqus are used to compare both methods (criteria). XFEM gives better results because it is capable of detecting the crack growth through the entire laminate, while the Hashin damage method can only predict the first ply failure and damage evolution (but no crack formation is allowed). In addition, the results show, as expected, a higher damage resistance in the plates dominated by 0º plies, since the loads are applied in this direction. Regarding to the different hole radii, it can be appreciated that the plates with smaller holes are stiffer, so they experience higher stresses for the same applied strain, which mean that they damage earlier.

Keywords: Fiber reinforced composites, plates, crack, damage, XFEM, Hashin criterion, finite element method**.**

Resumo

O principal objectivo desta tese consiste na modelação e simulação computacional do dano e rotura/falha de compósitos reforçados com fibras, utilizando o método dos elementos finitos. Durante o tempo de vida em serviço de uma estrutura aeroespacial, fendas e fissuração podem aparecer e sobretudo espalhar-se por todo o seu domínio. Estas situações devem ser analisadas com rigor de modo a determinar a influência que poderão ter na diminuição da rigidez e resistência da estrutura, a qual pode condicionar gravemente o seu desempenho.

Neste trabalho, procede-se a uma breve revisão da literatura relacionada com os diferentes estudos realizados nesta área de investigação, bem como a uma descrição sucinta de alguns métodos que permitem prever o começo e o crescimento das fendas. Ao longo deste trabalho, analisa-se o comportamento das placas compósitas com furos circulares usando o software Abaqus e dois métodos de análise: o método de *Hashin* e o XFEM ("eXtended Finite Element Method, na designação anglo-saxónica). O XFEM mostra grande capacidade de identificar o ínicio da fenda e a sua propagação em todo o laminado. O método baseado no criterio de Hashin não indetifica a fenda mas apenas o dano localizado, revertendo essas zonas danificadas com uma rigidez menor. Para além disso, os resultados mostram, como esperado, uma maior resistência das placas dominadas por lâminas a 0º, dado que as forças de tracção se aplicam nesta direção. É ainda possível concluir que as placas com furos menores são mais rígidas e exibem maiores tensões localizadas, facto que antecipa a sua falha.

Palavras-chave: Compositos de fibras, placas, fenda, dano, XFEM, Critério de Hashin, método dos elementos finitos.

Contents

List of Figures

List of Tables

Glossary

BVID (Barely Visible Impact Damage)

CDM (Continuum Damage Mechanics)

CFF (Compression Fiber Failure)

CFRP (Carbon Fiber Reinforced Plastic)

CMF (Compression matrix failure)

CS (Certification Specifications)

DDM (Discrete Damage Mechanics)

DOF (Degrees Of Freedom)

EASA (European Aviation Safety Agency)

ERR (Energy Release Rate)

FAA (Federal Aviation Administration)

FAR (Federal Aviation Regulation)

FE (Finite Element**)**

FEA (Finite Element Analysis)

FEM (Finite Element Method)

GFRP (Glass Fiber Reinforced Plastic)

JAA (Joint Aviation Authorities)

RVE (Representative Volume Element)

SFEM (S-Version Finite-Element Method)

SM (Safety Margin)

TFF (Tensile Fiber Failure)

TMF (Tensile Matrix Failure)

VID (Visible Impact Damage)

XFEM (eXtended Finite Element Method)

Nomenclature

Greek symbols

$\boldsymbol{\varepsilon}$	Strain tensor (plane stress).
ε_1	Strain in the direction 1 (direction of the fibers)
ε_2	Strain in the direction 2 (perpendicular to the fibers)
ε_{12}	Shear strain in plane 1-2
ε_{1Tu}	Ultimate tensile strain in the direction 1
ε_{1Cu}	Compressive ultimate strain in the direction 1
ε_{2Tu}	Tensile ultimate strain in the direction 2
ε_{2Cu}	Compressive ultimate strain in the direction 2
ε_{12u}	Ultimate shear strain in plane 1-2
σ_1	Stress in direction 1
σ_2	Stress in direction 2
τ_{12}	Shear stress
σ_{1u}	Ultimate stress in direction 1
σ_{2u}	Ultimate stress in direction 2
τ_{12u}	Ultimate shear stress
σ_{1u}^t	Ultimate tensile stress in direction 1
σ_{1u}^c	Ultimate compressive stress in direction 1
σ_{2u}^t	Ultimate tensile stress in direction 2
σ_{2u}^c	Ultimate compressive stress in direction 2
τ_{23u}	Interlaminar shear strength (in plane 2-3)
λ	Crack density
ϕ	Function phi, face of fracture
ψ	Function psi, forehead of initial fracture
$\Delta\lambda_k$	Increment of crack density
v_{12}	In-plane Poisson's ratio
v_{23}	Out-of-plane Poisson's ratio
Ω^G	Global mesh region in SFEM

Ω^L Local mesh region in SFEM

Roman symbols

a Crack length

a_I Nodal enrichment degrees of freedom (DOF)

A Crack area

b_I^α Nodal DOF vector

d Displacement

d_f Displacement at failure

E_1 Young modulus in the fiber direction

E_2 Young modulus in transversal direction

F Load

F_{max} Maximum load

F_{1t} Tensile strength in the fiber direction

F_{1c} Compressive strength in the fiber direction

F_{2t} Tensile strength in transversal direction

F_{2c} Compressive strength in transversal direction

F_6 Shear strength

F_α Crack tip asymptotic functions

G_{12} In-plane shear modulus

G_I Energy release rate in mode I

G_{II} Energy release rate in mode II

G_{Ic} Critical energy release rate in mode I

G_{IIc} Critical energy release rate in mode II

G_{cft} Critical energy release rate fiber tensile failure

G_{cmt} Critical energy release rate for matrix tensile failure

G_{cfc} Critical energy release rate for fiber compressive failure

G_{cmc} Critical energy release rate for matrix compressive failure

g(λ,ε) Activation function for DDM (function of crack density and strain)

H(x)	Heaviside distribution
k_1	Stress intensity factors in mode I
k_2	Stress intensity factors in mode II
K	Elastic stiffness
m	Weibull modulus
N_I	Shape functions
N_T	Nodes belonging to elements cut by crack
S	Surface energy
SM	Safety Margin
t_k	Lamina thickness
t_t	Transition thickness
U	Strain energy
$u(x)$	Displacement vector
u_I	Nodal displacement vectors
U_I	Strain energy for mode I
U_{II}	Strain energy for mode II

.

,

Chapter 1

INTRODUCTION

1.1 Generalities

Weight has always been an overriding concern when designing an aircraft. For this reason, different materials have been used throughout history, from simple wood to advanced composite materials.

Early in the aviation's history wood was the only viable material to build structures light enough to fly and also strong enough to withstand flight loads. However, this material had some problems like its degradation and its changes in size and properties caused by moisture. Due to its disposition in layers, wood behaves in a similar way to the composite materials that are dominating the current aircraft industry [1].

Two new aircrafts were developed in 1916 and 1918 respectively, the Junkers J1 and the Fokker D.VII, which included parts of aluminum and steel (Figure 1).

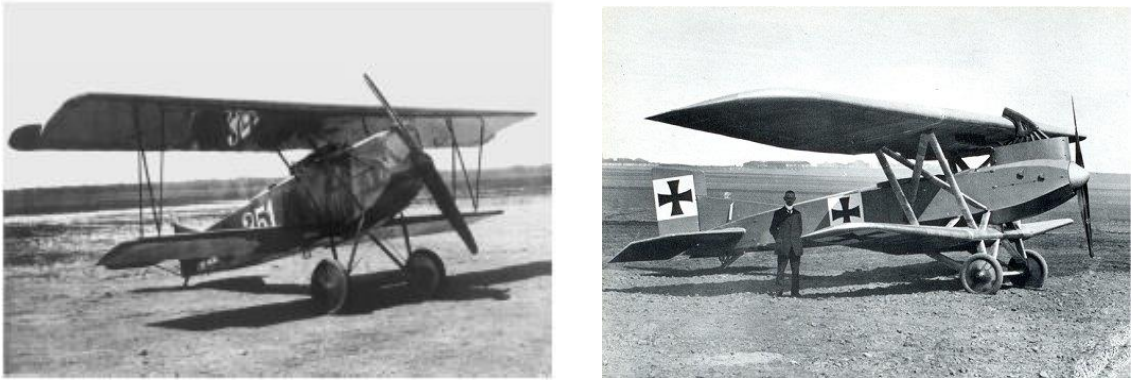

(a) (b)

Figure 1. Example of aluminum and steel aircrafts: (a) Junkers J1 and (b) Fokker D. VII [1]

In 1933 two new aircrafts were introduced in the industry, the Boeing 247D and the Douglas DC-3, which represented the embodiment of the structural revolution (Figure 2). They were totally manufactured in metal, that provided a high strength but at the expense of a higher weight. Steel provided excellent values of strength but the industry needed a lighter material, which is why since World War I, the development of its alloys led to a massive implementation of aluminum in aviation industry. It supplied a suitable strength, low density and ease of handling, forging and repair but with the limitations of aging and low tolerance to high temperatures.

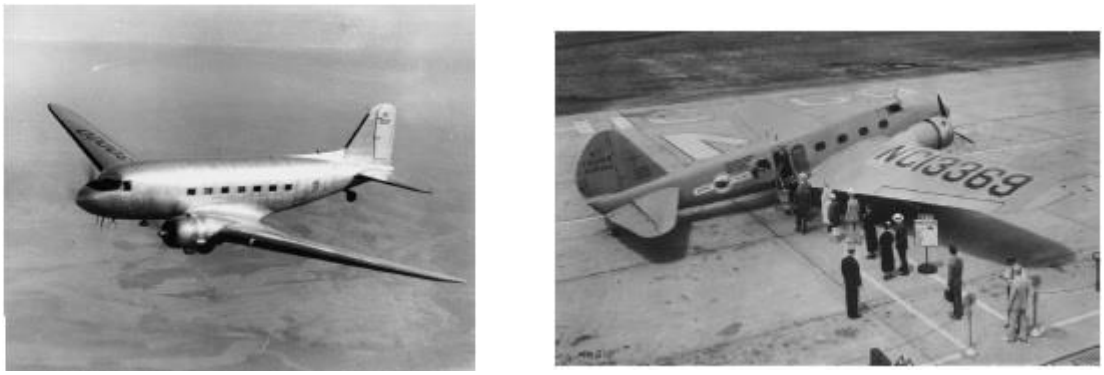

(a) (b)

Figure 2. Aircrafts totally manufactured in metal: (a) Boeing 247D and (b) Douglas DC-3 [1]

Titanium has a density between aluminum and steel, with an excellent resistance to corrosion and to high temperatures (400-500ºC), which makes it very useful for using in nozzles, coating for engines and highly heated areas. However, its high cost, which is seven times more expensive than aluminum, causes its use to be reduced to military applications. F117 and SR71 are some examples of titanium applications in military aircraft (Figure 3).

(a) (b)

Figure 3. Titanium applications in aircrafts: (a) Lockheed F-117 Nighthawk [2] and (b) Lockheed SR-71 [3]

The modern industry and most of all of the current developments and researches are focused on composites. These materials will be deeply analyzed in the next chapter.

1.2 Damage in aircrafts

Safety should be understood as a necessity, being supported by an extensive and complex certification regulation that forces to measure the deformation of aeronautical structures to make sure they support severe conditions without catastrophic failure. Therefore, the determination of the damage tolerance of the aeronautical structures is one of the targets of the certification processes.

During the service life of the aircraft, cracks and damages may appear over the aeronautical structures, which should be analyzed to determine the decrease of resistance that their presence involves. In addition, it is necessary to perform maintenance operations referred to in the aircraft maintenance manuals, in order to restore the level of resistance in a particular structure when the size of the damage exceeds a size that is fixed in the manuals.

Although the behavior of the damaged structures has been studied for decades, this is a relatively modern field of research. The need for designing damage tolerant structures and monitoring the health of the same ones arose in the 50s, through the establishment of a few appropriate protocols to perform the pertinent tests on the aircraft.

The above mentioned interest in the study of the damaged structures takes on greater importance as a result of the accidents of three Havilland Comet planes that occurred in 1953 and 1954. On May 2nd, 1953 one Havilland Comet [4] departed from Calcuta to Delhi but shortly after taking-off and going through a strong storm, the plane collapsed. A few months later, on January 10th, 1954 another Comet which covered the route between Rome and London crashed and the causes of the accident were unknown. A third accident on April 8th, 1954 where another comet that covered the route Rome-El Cairo collapsed in similar conditions as the previous two, led to the suspension of the fleet and the development of tests to determine the causes of the accidents. After carrying out tests on the Comets, it was determined that the cause of the disaster had been the growth of fatigue cracks in the structure near the windows (Figure 4).

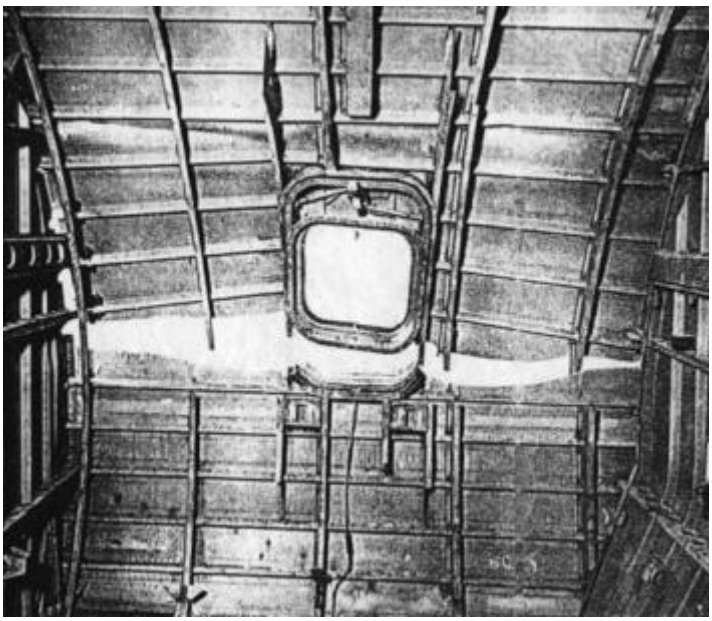

Figure 4. Crack in the window of a Havilland Comet [4]

Another important and very well-known failure in the structure of an airplane in service was the flight 243 of Aloha Airlines [5] (Figure 5). The aircraft took off on April 28th, 1988 from Hilo to cover the

route between this city and Honolulu but some minutes later, the roof and a big part of the side fuselage of the front section become detached leaving the airplane completely depressurized. After a long investigation, it was determined that the cause of the accident was the fatigue of the metal caused by the vibrations origin that were generated in each take-off cycle, having exceeded the allowable cycles.

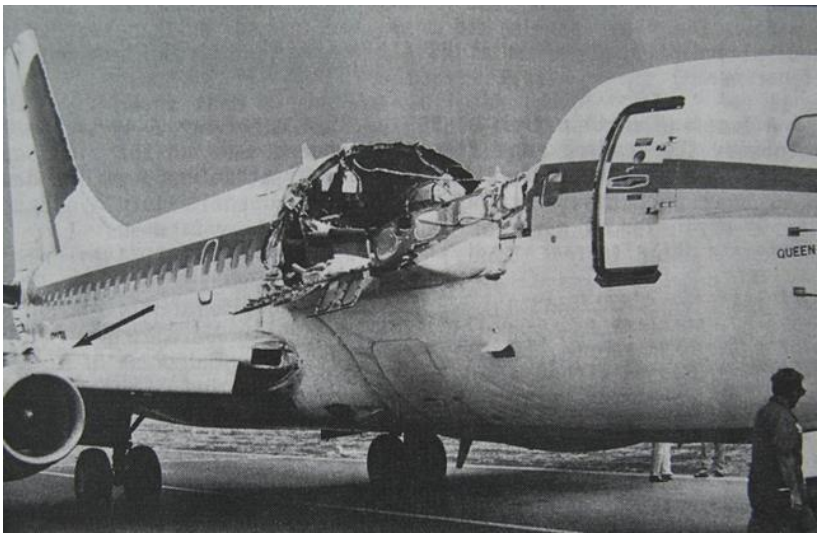

Figure 5. Flight 243 Aloha Airlines after the detachment of the fuselage [5]

In case of failures related with composite material structures, it is possible to quote the accident of the flight 961 of air Transat [6] (Figure 6), on March 6th, 2005, in which the rudder of the Airbus A310-308 detached in flight. The following investigation showed that the failure was caused by a gap into the composite structure that after many cycles of changing pressure, it had grown and finally exploded. The rudder lost strength and stiffness, it started "fluttering" and broke up.

Figure 6. Different views of the detachment of the rudder of Air Transat flight [6]

In order to try to avoid these catastrophic failures, there is a clear need to correctly determine both the structures that are likely to fail as the need to regulate adequately the tests that are performed on the aero structures, evolving the processes of certification and testing of the aircraft.

Currently there are some strict criteria for obtaining the two necessary documents for an aircraft can fly, which are the type certificate and the airworthiness certificate. Having in each country (or group of countries) an authority in charge of aircraft certification, being the most important organism worldwide the European EASA (European Aviation Safety Agency) and the American FAA (Federal Aviation Administration).

EASA is a specific organism belonging to European Union that has law and executive power, replacing the old JAA (Joint Aviation Authorities). Among its many duties, it highlights the emission of the “Type certificates” as described in the 1703/2003 regulation of the European Union, from which arise the “Certification Specifications” known as CS standards. The FAA is the organization in charge of issuing the certificates in United States, relying on the FAR (Federal Aviation Regulation) standards.

According to Ilcewicz [7], once a damage threat assessment is completed, there are 5 different categories of damage and defect considerations for primary composite aircraft structures as described below [7-8] (Figure 7):

- ***Category 1***: allowable damage that may go undetected by scheduled or directed field inspection. For example: barely visible impact damage (BVID), minor environmental degradation, scratches, gouges and allowable defects that must retain ultimate load for the specified life.
- ***Category 2***: Damage detected by scheduled or directed field inspection at specified intervals. For example: visible impact damage (VID), deep gouges or scratches, manufacturing mistakes not evident in the factory, detectable delamination or debonding, and major local heat or environmental degradation that will sustain sufficient residual strength until found.
- ***Category 3***: Obvious damage detected within a few flights by focal operations. For example: damage obvious to operations in a “walk-around” inspection or due to loss of form/fit/function that must retain limit load until found by operations.
- ***Category 4***: Discrete source damage known by pilot to limit flight maneuvers. For example: damage in flight from events that are obvious to pilot (rotor burst, bird-strike, lightning, exploding gear tires, severe in-flight hail).
- ***Category 5***: Severe damage created by anomalous ground or flight events. For example: damage occurring due to race service events or to an extent beyond that considered in design, which must be reported by operations for immediate action.

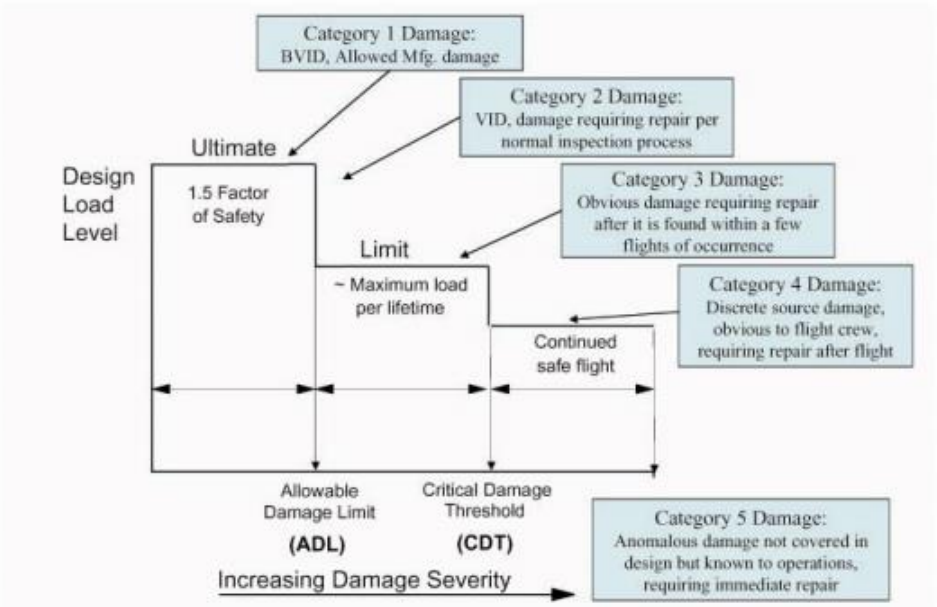

Figure 7. Categories of damage for composites in aircraft [9]

1.3 Motivation and objectives

The Fracture Mechanics attempts to answer questions about the behavior of the structures that have cracks and their resistant ability after suffering damage. It's a relatively modern field within the structural engineering, being more and more important the prediction of the behavior of certain damaged structures. The need for an extensive knowledge of the Fracture Mechanics is critical in the aerospace industry where the in-service behavior of damaged structures must be demonstrated like indispensable requisite.

Consistently, multiple studies have been carried out, based on analytical, numerical and computational techniques, to deal with the problem of the cracks in a way closer to the reality. Numerical and computational techniques are supported with the exponential growth of the available calculation resources, allowing to solve more complex problems and to better fit the parameters that characterize modern Fracture Mechanics. In this case, the Finite Element Method (FEM) is an extremely useful computational technique to determine the stiffness and strength of a damaged structure.

Composite materials have meant a breakthrough for the aerospace industry, while they improve many of the behaviors of the aeronautical structures where they are used, for instance the improvement of the corrosion behavior, the increase of fatigue resistance or the decrease of self-weight. The fact of being a field in constant evolution and growth is what has led to the election of this project, since composite structures is a very important area with continuous evolution.

On the other hand, most of the documents that have been consulted (related with the damage in composite materials in aero structures and the presence of cracks in them) did not include experimental validation of numerical results. All this, joint with the little information and studies done

for the analysis of the cracks in composite materials through the eXtended Finite Element Method (XFEM), have also been important factors to take into account for the choice of this project.

1.4 Thesis Outline

This thesis consists of six chapters which are organized as follows:

- Chapter 1 includes a little review about the different materials used in the aviation industry throughout the history. Some cases of damage in aircraft are presented in order to show the importance of the study of the onset of the damage in aircraft structures. Finally the motivations and the targets of this project are exhibited at the end of the chapter.
- In Chapter 2 a full review of composites materials is presented. The main concepts about these materials are presented as well as the different applications in aviation (commercial and military) and the future trends in using them in the next few years.
- Chapter 3 describes the different methods available to predict damage in composite materials. Some of them only will predict the first ply failure as “Failure Criteria” while others will predict the damage evolution through the entire laminate as “Continuum Damage Mechanics” (CDM) and “Discrete Damage Model” (DDM).
- In Chapter 4 three previous studies on composite damage are presented.
- Some parametric studies are carried out in Chapter 5 in order to compare the different results obtained after using the both XFEM and Hashin-based methods. Plates with different hole radii and stacking sequences are analyzed during these parametric studies.
- Finally, Chapter 6 presents the main conclusions and future recommendations.

Chapter 2

COMPOSITES

2.1 Historical background

The concept of composite material is as old as nature itself. An example of that is in the wood, in which, the cellulose fibers are joined by an array of lignin. In the cases of bones, there are also reinforced and stiffened structures with fibers. Adobe and straw bricks constitute another example of composite material. However, the concept of composite material relating to current technology didn't start to develop until the end of the 19th century. In 1878, T. A. Edison produces carbon filaments from human hair and mane of horse to use them like filaments in incandescence lamps. In the 30's of the 20th century, the polyester resin is invented and continuum glass fibers begin to be produced in Japan, which ends with the construction of the first boat built from glass fiber and polyester resin in 1942.In 1952 the researches about graphite filaments start to take place in the "Royal Aerospace Establishment" in England giving rise, in 1959, to the development of high resistance graphite fibers in Japan. Thereafter, all of these materials begin to be introduced in military aircrafts. It takes place, in 1970, the first flight of the Grumman F-14, an aircraft which was provided with coatings of the horizontal stabilizer built with boron/epoxy composite material. In 1974 takes place the first flight of the General Dynamics F-16, aircraft whose coatings of the stabilizers were built with carbon/epoxy composite material. The McDonnell-Douglas company also begins to make use of carbon/epoxy composite material in coatings of wing, stabilizers, stringers of the wing and rear fuselage since 1980 in its military aircraft F/A-18 and AV-8B. In the field of commercial aviation will have to wait until 1988 with the commissioning of the Airbus A320, first commercial aircraft in using carbon/epoxy composite material in its primary structure, more specifically in the stabilizers. With the first flight of the Airbus A380, in 2005, these composites will play a most remarkable role, comprising 25% in weight of the aircraft structure. Although, the real revolution arrived with the Boeing B787 (Figure 8)

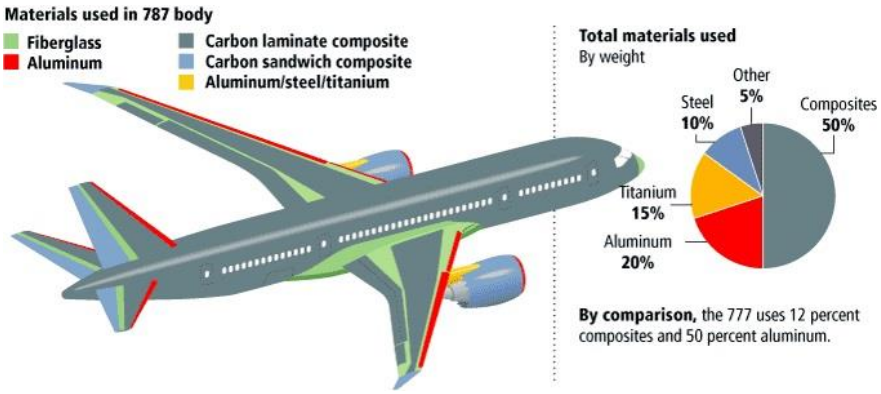

Figure 8. Materials in Boeing 787 [10]

and Airbus A350, where the composite material reaches, respectively, 50% and 52% of the weight of the structure, including wing and fuselage.

2.2 Concepts and advantages

Composite materials are based on a combination of different materials that are combined together to obtain specific structural properties. The individual materials do not dilute or merge completely in the composite, but they have the ability to behave together as one. Normally, the matrix and fibers can be physically recognized as they interface with one another. The properties and features of the composite material are higher and better than the properties of the individual materials from which it is built. An advanced composite material is made of a fibrous material embedded in a resin matrix. This whole of fibers and matrix makes up the plies, which are usually oriented in different directions to give to the material the necessary strength and stiffness. Fibrous materials have been present in the nature since the beginning of the times; wood is the most common fibrous structural material known to man [11].

The strength and the stiffness of a composite material reside in the direction of the fibers. The main purpose of the fibers is to bear the load while the matrix supports the fibers and bond them together. The function of the matrix is to transfer any applied loads to the different fibers, keeps the fibers in their natural position and chosen orientation, control the impact strength and damage tolerance, and give the composite environmental resistance (durability). The stacking sequence of the plies describes the distribution of ply orientations through the laminate thickness. The structural properties of the composite material depend on the stacking sequence of the plies that have been selected. Strength, stiffness and dimensional stability have a huge influence of the stacking sequence [11].

It is needed to select a proper orientation in advanced composite materials to guarantee a structurally efficient design. 0º plies are required to support axial loads, 90º plies to support side loads and ±45º plies to support shear loads. Quasi-isotropic layups are typical in many aerospace composite structures. This type of laminate consists in a 0º, -60º, +60º sequence or in a 0º, -45º, +45º and 90º sequence, with the same number of plies following that sequences (Figure 9).

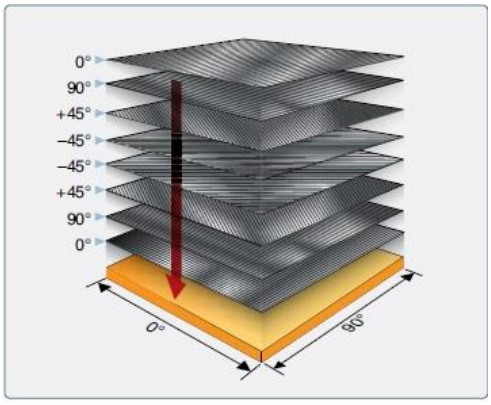

Figure 9. Quasi-isotropic layup [11]

The increasing use of composite materials is due, among other reasons, to their low weight, high stiffness- and strength-to-weight ratios, good fatigue behavior, corrosion resistance and can be constructed to fulfill a predefined strength or performance objective. Composites allow radar signals pass through them, for this reason composites are perfect materials for using wherever radar equipment is operating, both in the air and ground. Composites are very important in stealth aircraft, such as the U.S. Air Force's B-2, which is nearly transparent to radar. However, there are some limitations since they are vulnerable to cracking and interlaminar delamination. High price of the final product, repair difficulties, low resistance between sheets, lack of knowledge regarding their behavior in some aspects, absence of permanent plastic deformation (low ductility) and brittleness are some others problems that these materials may have. But without a doubt, the main limiting factor is the absence of damage tolerance. Small impacts cause almost imperceptible delamination that produces a high loss of their mechanical resistance.

2.3 Fiber and matrix types

Fibers

Fiber is the reinforcing element by excellence supporting and transmitting loads along its direction. Most common fibers used for composite materials are Fiberglass, Carbon/Graphite, Kevlar and Boron.

- ***Fiberglass***

Glass is an amorphous material, with virtually no crystalline structure, mainly composed by silicon oxides and other metallic oxides that, according to the proportion in which they are present, these give to the glass a few certain characteristics. In a general way, fiberglass (Table 1) presents good tensile and impact resistance, galvanic or chemical corrosion resistance, lower cost than other composite materials and electrical properties (fiberglass does not conduct electricity). This type of composite fibers is commonly used for secondary structure on aircrafts, such as radomes, fairings and wing tips; it is also used for helicopter rotor blades [12].

Table 1. Fiberglass properties

Property	**E-Glass**	**S-Glass**
Density [g/cm^3]	*2,55-2,58*	*2,46-2,49*
Modulus [GPa]	*70-72*	*86-91*
Strength [GPa]	*3400*	*4500*
Strain [%]	*4,5-5*	*5,4-5,8*
Thermal expansion coefficient [10E-06 ºC^{-1}]	*5,5*	*1,6*
Fiber diameter [µm]	*4 to 25*	*5 to 9*

The most common types of fiberglass used for composite materials are the electrical glass, or E-glass and the structural glass, or S-glass.

- ***Carbon/Graphite***

One of the first distinctions to be made among fibers is the difference between graphite and carbon fibers, although the terms are often used interchangeably. Actually, carbon and graphite fibers present differences in their chemical structure and carbon (C) content. Having the carbon fibers a tensile modulus lower than 380 GPa and the graphite fibers higher, but this does not happens always as well. In a general way, carbon fibers present high strength and corrosion resistance, being its stiffness 3 to 10 times higher than glass fibers. Its Aquiles's heel is their high sensibility to the impact damage and its high cost. Carbon fibers are obtained from three different types of precursors: (i) PAN (polyacrylonitrile), (ii) tar (pitch) and, in a much smaller proportion, (iii) rayon (regenerated cellulose). This type of composite fibers is used for structural aircraft applications, such as stabilizers, floor beams, primary fuselage and wing structure and flight controls (Table 2) [12].

Table 2. Carbon fibers properties

Property	**PAN Precursor**				**Tar Precursor**	
	Standard modulus	**Intermediate modulus**	**High modulus**	**Ultra high modulus**	**Structural**	**Thermally Conductive**
Density [g/cm^3]	*1,76*	*1,76*	*1,91*	*2,0-2,25*	*2,15*	*2,10-2,20*
Modulus [GPa]	*228,248*	*290-310*	*320-440*	*440-1000*	*170-830*	*965*
Strength [MPa]	*3500-4830*	*4100-6900*	*3500-4000*	*2000-3200*	*2000-2450*	*1720-1900*
Strain [%]	*1,5*	*1,8*	*0,8*	*0,2-0,3*	*0,3-0,5*	*0,25*
Thermal expansion coefficient [10E-06 ºC^{-1}]	*-0,5*	*-0,5*	*-0,9*	*-1,5*	*-2,7*	*-3,1*
Thermal Conductivity [Z/mK]				*40-75*	*10-600*	*1100+*

- ***Kevlar***

Kevlar® is DuPont's name for aramid fibers. This type of fibers have a high resistance to impact damage, they are strong, light weight and tough, offering the best properties in damage tolerance of all fibers available. But these fibers present some disadvantages like susceptibility to degradation by UV radiation and large absorption of moisture by the fiber which means weight increases of the order of 7-8%. Two types of Kevlar fibers can be distinguished in aviation industry: (i) Kevlar® 49, which has a high stiffness and (ii) Kevlar® 29, which has a low stiffness. Most common application of Kevlar are military ballistic and body armor applications (Table 3) [12].

Table 3. Kevlar properties

Property	**Du Pont manufacturer**	
	Kevlar 29	**Kevlar 49**
Density [g/cm^3]	*1,44*	*1,45*
Modulus [GPa]	*70-83*	*112-124*
Strength [MPa]	*2760-3620*	*2760-3620*
Strain [%]	*3,6*	*2,4*
Thermal Expansion Coefficient [10E-06ºC^{-1}]	*-4*	*-2*
Fiber Diameter [µm]	*12*	*12*

- ***Boron***

Boron fibers stand out by its high compression resistance, joined to its high tensile and compressive elastic modulus. The fibers are very stiff and have a large diameter, being only available as a prepeg tape product. Its high price and the fact that are usually difficult to mechanize are some of its disadvantages. So this type of fibers is used primarily in military aviation applications (Table 4) [12].

Table 4. Boron properties

Property	**Boron**
Density [g/cm^3]	*2,38-2,54*
Modulus [GPa]	*400*
Strength [MPa]	*3585-4000*
Thermal Expansion Coefficient [10E-06 ºC^{-1}]	*4,5*
Fiber Diameter [µm]	*76-142*

Matrix

The purpose of the matrix in a composite material is to transfer and redistribute loads towards and between reinforced fibers. It also maintains the fibers with the correctly orientation, protects the fibers of the environment and provides resistance to interlaminar shear, compressive strength and transverse resistance. Matrix is also the responsible of determining the processability and the maximum service temperature of the composite material. It is possible to distinguish between polymerics, metallics and ceramics matrix. The most widely used and interesting are the first ones. Polymeric matrix could divide between thermosetting and thermoplastic. Thermosettings are presented without polymerization, doing it during the manufacturing process of the final piece while thermoplastics are presented in solid state polymerized already. A brief description of some of the most common thermoset resins will be done below.

- ***Polyester Resins***

Polyester resins are generally inexpensive, with a quick manufacturing process that allow them to be used generally for low cost applications like interior parts of the aircraft. Some of the most common processing methods for the fiber-reinforced polyesters include wet layup, press molding, pultrusion, filament winding and autoclaving [12].

- ***Vinyl Ester Resin***

This kind of resin has similar features to those of the polyester resins in terms of appearance, handling properties and curing. However, vinyl ester resins have better mechanical properties and corrosion resistance than the usual polyester resins and its strength and bulk cost is between polyester and epoxy [12].

- ***Phenolic Resin***

Phenolic resins present lower mechanical properties than epoxy but with a good resistance to high temperatures (>250ºC), good dimensional stability, and low smoke and flammability characteristic. The above mentioned allows them to be used for interior components of the aircraft [12].

- ***Epoxy***

Epoxies are polymerizable thermosetting resins being available from liquid to solid. Their properties depend on the basic resin, the curing agent, the added modifiers and the polymerization conditions. The main advantages of these resins are high mechanical properties with a service temperature between 60 and 150ºC, low thermal shrinkage, good chemical resistance, low levels of volatiles and ease of processing. While some of their disadvantages are their bad behavior under the presence of moisture, and their brittleness. Therefore, most common applications of epoxy resins are for structural adhesives and resins for prepreg materials [12].

2.4 Evolution of composites used in aviation industry

Some data, statistics and graphics are presented below, in order to obtain a more detailed insight about the evolution experienced by composite materials and their use in the aviation industry. Figure 10 shows the data relating to commercial aviation, noting a clear evolution from the first decade of the 21st century.

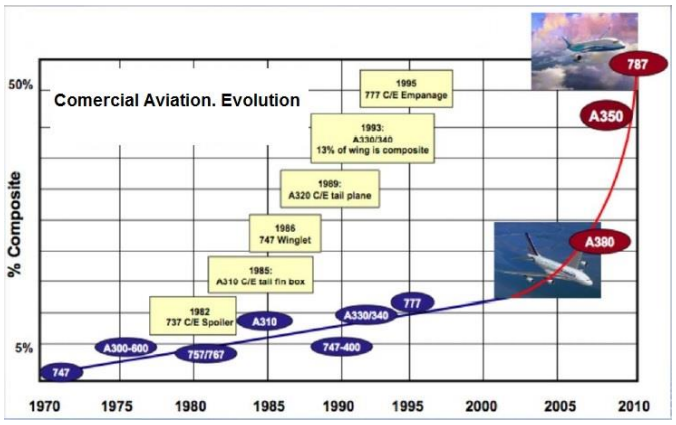

(a)

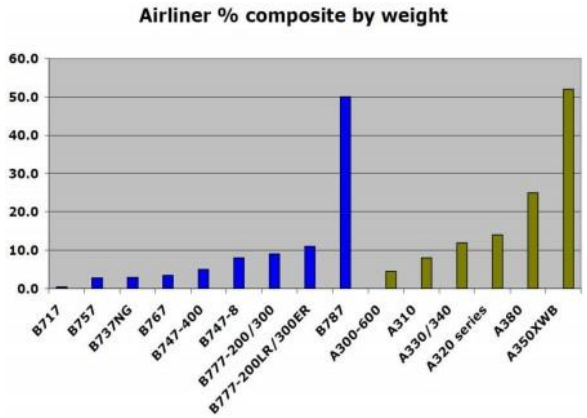

(b)

Figure 10. Composites evolution in commercial aircraft: (a) [12], (b) [12]

Presenting a more concrete example in Figure 11, showing the full evolution of the aircrafts developed by the manufacturer Airbus. It can be appreciated the evolution followed by this manufacturer from their first models, which used composite materials only for small parts like flaps, spoilers and

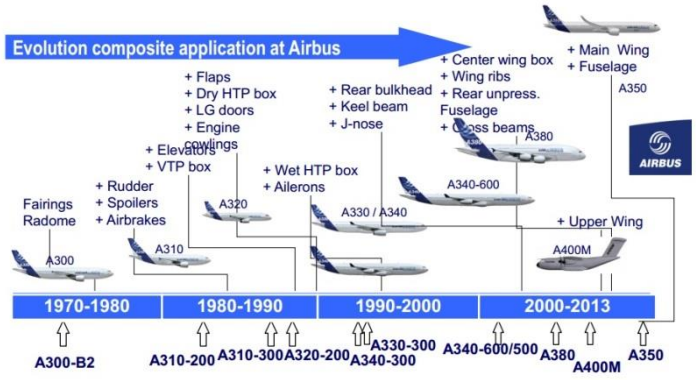

Figure 11. Evolution of composite application at Airbus [12]

radomes, to the latest models which include the composite materials in large sections of their fuselage.

Figure 12 is referred to the case of military aviation, where the evolution has been more linear than in the case of the commercial aviation. This is because the military planes have always been provided with the most top technology, being the composite materials included in this top technology.

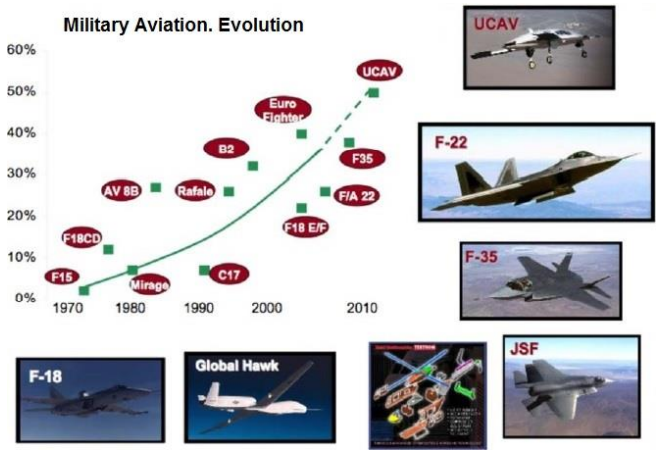

(a)

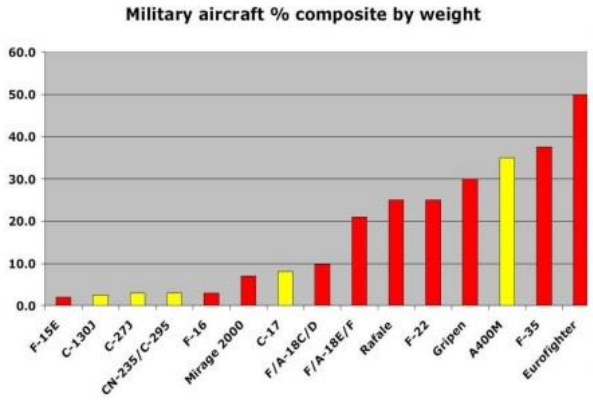

(b)

Figure 12. Evolution of composites in military aviation: (a) [12], (b) [12]

As an example of the distribution of the different types of composite materials in a military aircraft, it is shown as a guideline the Figure 13 corresponding to an Eurofighter Typhoon. Almost the whole fuselage is made of carbon fiber reinforced plastic (CFRP), while the use of glass fiber reinforced plastic (GFRP) is reduced to the radome and a piece of the vertical tail. Likewise, it can be observed a small use of titanium and aluminum in small parts of the aircraft such as stabilizers, ailerons, slats and the nozzles.

Figure 13. Distribution of composite materials in Eurofighter Typhoon [12]

The global market of composite materials in 2011 supposed 19600 million US Dollars, being estimated that it can reach 30000 million in 2017 (Figure 14). In this amount, only around 10% corresponded to advanced composite materials, but this percentage is estimated to grow significantly over the next decade due to the increasing demand of the aerospace, defense, transport and wind energy sectors. Growth will be high in developing nations such as India, China, Russia and Brazil. The global market of carbon fiber-reinforced composite materials reached in 2012 a volume of 10000 million US Dollars and it is estimated that it could reach the 40000 million in 2022 (Figure 14), which has caused in the last years a series of procurement operations, unions and "joint ventures" of different actors of the productive market of carbon fibers, looking for a better position facing the increasing demand of fibers and fibrous reinforcement products.

The strong growth for the aerospace composite materials market, especially in the segment of commercial aircrafts, is due to

- a better understanding of the behavior and capabilities of the composite materials,
- the growing demand of lighter and more efficient aircrafts from the point of view of fuel savings, and
- the improvement and optimization of the manufacturing processes of composite materials structures.

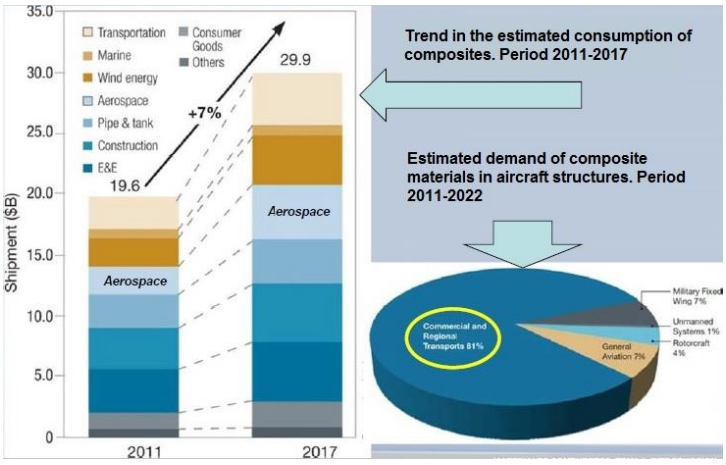

Figure 14. Future trends in use of composites [12]

It is predicted an expansion of the air flights and their importance will be strongly linked to maintain the safety for air transportation and the need for the airlines to reduce operating costs. Both aspects will shape the composite aeronautical materials industry in the next years.

Chapter 3

DAMAGE MODELS

3.1 Failure criteria

The failure mechanism of the advanced composite materials and, therefore, their sensitivity to breakage, durability and damage tolerance are radically different from those of the metallic materials. General failure is preceded by failure phenomena that happen on a microscopic level such as: matrix microcracking, matrix creep, separation of the matrix/fiber interface, and delamination [12].

This section will discuss the most commonly used criteria, although with these criteria there is no information about crack evolution when the composite material fails.

There are two main groups of failure criteria in composite materials: (i) failure criteria not associated with failure modes and (ii) failure criteria associated with failure modes [13]. Those of the first group are usually polynomial criteria while the second ones propose different equations depending on the mechanism of breakage. Within the failure criteria not associated with failure modes will be presented the Tsai-Hill and Tsai-Wu criteria; while regarding to the failure criteria associated with failure modes, there will be reference in this section to the maximum strain criterion and the Hashin criterion [12].

3.1.1 Maximum strain criterion

This criterion is based on supposing that the failure takes place when some of the strains of the lamina exceed the allowable deformation, being a simple and direct way to predict failure of composites. So they can be considered three different failure conditions in correspondence with an ultimate strain in fiber direction, matrix or transversal direction and for shear strains [14]:

- *Fiber:* $\varepsilon_1 \geq \varepsilon_{1Tu}$ *or* $|\varepsilon_1| \geq \varepsilon_{1Cu}$
- *Matrix:* $\varepsilon_2 \geq \varepsilon_{2Tu}$ *or* $|\varepsilon_2| \geq \varepsilon_{2Cu}$
- *Shear:* $|\varepsilon_{12}| \geq \varepsilon_{12u}$

Where subscript u means ultimate, ε_1 is the strain in the direction 1 (direction of the fibers of each ply), ε_{1Tu} is the ultimate tensile strain in the direction 1, ε_{1Cu} is the ultimate compressive strain in the direction 1, ε_2 is the strain in the direction 2 (perpendicular to the fibers direction), ε_{2Tu} is the ultimate tensile strain in the direction 2, ε_{2Cu} is the ultimate compressive strain in the direction 2, ε_{12} is the shear strain in plane 1-2 and ε_{12u} is the ultimate shear strain in plane 1-2. When one of these three conditions appears, failure will occur.

3.1.2 Tsai-Hill criterion

This criterion [15] is based on the elasticity theory of anisotropic materials developed by Hill. There will be no failure while the failure index (I_f) is lower than the unity, meaning that a given point of the structure is safe if [12, 15]:

$$I_f = \left(\frac{\sigma_1}{\sigma_{1u}}\right)^2 + \left(\frac{\sigma_2}{\sigma_{2u}}\right)^2 + \left(\frac{\tau_{12}}{\tau_{12u}}\right)^2 - \frac{\sigma_1\sigma_2}{\sigma_{1u}^2} \leq 1 \quad (1)$$

where σ_1 is the stress in direction 1, σ_{1u} is the ultimate stress in direction 1 (maximum strength in direction 1), σ_2 is the stress in direction 2, σ_{2u} is the ultimate stress in direction 2 (maximum strength in direction 2), τ_{12} is the shear stress in plane 1-2 and τ_{12u} is the ultimate shear stress in plane 1-2 (maximum shear strength in plane 1-2). A possible measure of the safety margin (SM) could be given by [12]

$$SM = \left[\left(\frac{\sigma_1}{\sigma_{1u}}\right)^2 + \left(\frac{\sigma_2}{\sigma_{2u}}\right)^2 + \left(\frac{\tau_{12}}{\tau_{12u}}\right)^2 - \frac{\sigma_1\sigma_2}{\sigma_{1u}^2}\right]^{-\frac{1}{2}} - 1 \quad (2)$$

3.1.3 Tsai-Wu criterion

Tsai and Wu presented in 1971 [16] a general theory of the strength of the anisotropic materials that established the hypothesis of the existence of a failure surface represented by a “scalar failure criteria function”, in the following way [12, 16]:

$$f(\sigma_k) = F_i\sigma_i + F_{ij}\sigma_{ij} = 1 \quad (3)$$

where i, j, k=1…6 and F_i and F_{ij} are strength tensors related to the lamina strengths in the principal directions. So that this criterion dictates that there will be no failure while $f(\sigma_k) \leq 1$.

Neglecting the higher order terms of the strength tensor, considering orthotropic materials and bearing in mind some additional simplifications (plain stress level, symmetry, lack of interaction between normal and shear stresses) the number of coefficients comes down to 6 and Tsai-Wu criterion is given by [12, 16]

$$F_1\sigma_1 + F_2\sigma_2 + F_{12}\sigma_1^2 + 2F_{12}\sigma_1\sigma_2 + F_{22}\sigma_2^2 + F_{66}\tau_{12} \leq 1 \quad (4)$$

$$F_1 = \frac{1}{\sigma_{1u}^t} - \frac{1}{\sigma_{1u}^c} \quad (5)$$

$$F_2 = \frac{1}{\sigma_{2u}^t} - \frac{1}{\sigma_{2u}^c} \quad (6)$$

$$F_{11} = \frac{1}{\sigma_{1u}^{t}\sigma_{1u}^{c}} \quad (7)$$

$$F_{22} = \frac{1}{\sigma_{2u}^{t}\sigma_{2u}^{c}} \quad (8)$$

$$F_{66} = \frac{1}{\tau_{12u}^{2}} \quad (9)$$

$$F_{12} \cong 0 \quad (10)$$

where σ_{1u}^{t} is the ultimate tensile stress in direction 1 (maximum tensile longitudinal strength), σ_{1u}^{c} is the ultimate compressive stress in direction 1 (maximum compressive longitudinal strength), σ_{2u}^{t} is the ultimate tensile stress in direction 2 (maximum tensile transversal strength) and σ_{2u}^{c} is the ultimate compressive stress in direction 2 (maximum compressive transversal strength).

In the same way that happened with the Tsai-Hill criterion, Tsai-Wu also establishes a safety margin, which could be obtained with the following expression:

$$(SM + 1)^2 A + (SM - 1)B - 1 = 0 \quad (11)$$

Where A and B are given by the next two formulas:

$$A = F_{11}\sigma_1^2 + F_{22}\sigma_2^2 + F_{66}\tau_{12} \quad (12)$$

$$B = F_1\sigma_1 + F_2\sigma_2 \quad (13)$$

It is important to understand that the failure criteria that are not based on the failure modes (as in the case of polynomial Tsai-Wu and Tsai-Hill criteria) are purely empirical, and its objective is to define a failure envelope using the minimum number of data.

3.1.4 Hashin criterion

Hashin [17] proposed that the criterion to predict the failure of a composite material must necessarily be based on the failure mechanisms of the material instead of being simply an extrapolation of existing criteria for other materials such as in the previous cases (Tsai-Hill, Tsai-Wu…). This failure criterion is used for predicting different failure modes as fiber breakage in tension, fiber buckling in compression, matrix cracking and debonding.

Under this idea, the author initially proposed a criterion for a biaxial stress state (Hashin-Rotem, 1973, [18]), and later a second criterion for three-dimensional stress states (Hashin 1980, [17]). The assumptions on which Hashin based his originals proposals are the following ones:

- Separated consideration of the different failure modes:

  - *Fiber failure*: tension and compression.
  - *Matrix failure*: tension and compression.

- The interaction between the different components that are involved in a failure mode is chosen quadratic.

The expressions of these criteria after making some bi-dimensional simplifications ($\sigma_3 = \tau_{13} = 0$) are shown below, where damage initiation occurs when any of these indexes exceeds "1.0":

Hashin-Rotem criterion, (1973) [18]

- Tensile fiber failure (TFF) $\frac{\sigma_1}{\sigma_{1u}^t} = 1 \quad (\sigma_1 > 0)$ (14)

- Compression fiber failure (CFF) $\frac{|\sigma_1|}{\sigma_{1u}^c} = 1 \quad (\sigma_1 < 0)$ (15)

- Tensile matrix failure (TMF) $\left(\frac{\sigma_2}{\sigma_{2u}^t}\right)^2 + \left(\frac{\tau_{12}}{\tau_{12u}}\right)^2 = 1 \quad (\sigma_2 > 0)$ (16)

- Compression matrix failure(CMF) $\left(\frac{\sigma_2}{\sigma_{2u}^c}\right)^2 + \left(\frac{\tau_{12}}{\tau_{12u}}\right)^2 = 1 \quad (\sigma_2 < 0)$ (17)

Hashin criterion, (1980) [17]

- Tensile fiber failure $\left(\frac{\sigma_1}{\sigma_{1u}^t}\right)^2 + \left(\frac{\tau_{12}}{\tau_{12u}}\right)^2 = 1 \quad (\sigma_1 > 0)$ (18)

- Compression fiber failure $\frac{|\sigma_1|}{\sigma_{1u}^c} = 1 \quad (\sigma_1 < 0)$ (19)

- Tensile matrix failure $\left(\frac{\sigma_2}{\sigma_{2u}^t}\right)^2 + \left(\frac{\tau_{12}}{\tau_{12u}}\right)^2 = 1 \quad (\sigma_2 > 0)$ (20)

- Compression matrix failure $\left(\frac{\sigma_2}{2\tau_{23u}}\right)^2 + \left[\left(\frac{\sigma_{2u}^c}{2\tau_{23u}}\right)^2 - 1\right]\frac{\sigma_2}{\sigma_{2u}^c} + \left(\frac{\tau_{12}}{\tau_{12u}}\right)^2 = 1 \quad (\sigma_2 < 0)$ (21)

where σ_3 is the stress in direction 3, τ_{13} is the shear stress in plane 1-3, τ_{23} is the shear stress in plane 2-3 and τ_{23u} is the interlaminar ultimate shear strength in plane 2-3 (maximum shear strength in plane 2-3).

In what refers to the tensile fiber failure, in the Hashin criterion of 1980 [17] it is included the contribution to the failure of the stress component τ_{12} however, for the compression fiber failure and the tensile matrix failure the expression does not change with respect to the previous Hashin-Rotem criterion of 1973 [18]. For the prediction of the compression matrix failure, the expressions used for Hashin-Rotem criterion of 1973 [18] and Hashin criterion of 1980 [17] differ [18, 19].

In spite of starting from the assumption that the stress components in the failure plane are responsible of the failure, Hashin [17] proposed a quadratic interaction due to the difficulty of determining the failure plane and the mentioned stress components. In the figure below [19], Figure 15, the two Hashin criteria are compared with the experimental data taken from Jones [20] for a glass-epoxy composite material for both tension and compression loading; where this tension data are represented by solid circles, and the compression data by solid squares. Likewise, the four different Hashin failure modes: (i) TFF, (ii) CFF, (iii) TMF and (iv) CMF are denoted by the blue, pink, red and green solid curves respectively. It is noted that both criteria are consistent with the data, even improving the Tsai-Hill approach for compression failure.

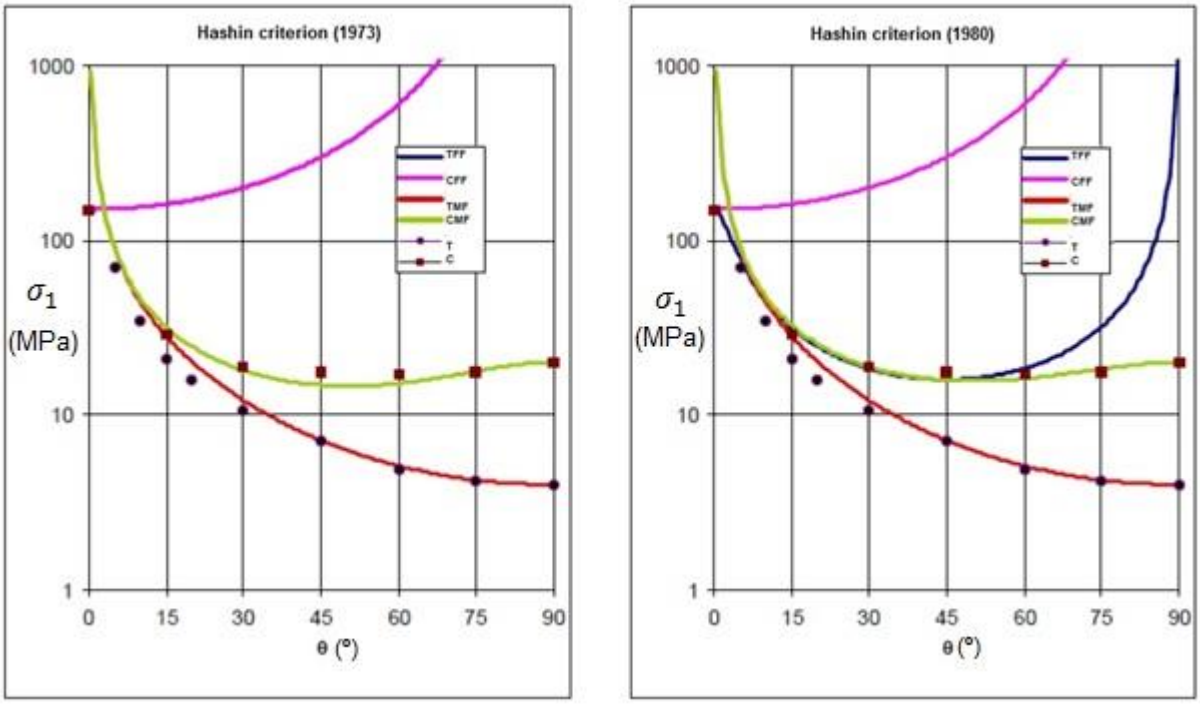

(a) (b)

Figure 15. Comparison between experimental results and the Hashin criteria [19]: (a) Hashin-Rotem (1973) [18], (b) Hashin (1980) [17]

3.2 Degradation models

The failure criterion dictates the conditions for which it is predicted that a material damage will occur and the degradation model is a mathematical representation of the mechanical properties of the material after being damaged.

According to this model, the part of the "damaged" material will be downloaded redistributing the load between the undamaged material. This process will be repeated until no more load could be supported and then the laminate will have reached the failure. One of the main goals of a degradation model is to correctly characterize the stiffness of the damaged material. The degraded property and the amount in which this property is reduced obviously will depend on the failure mode. In Figure 16 there is an example of the crack appearance and its subsequent propagation and laminate degradation [21].

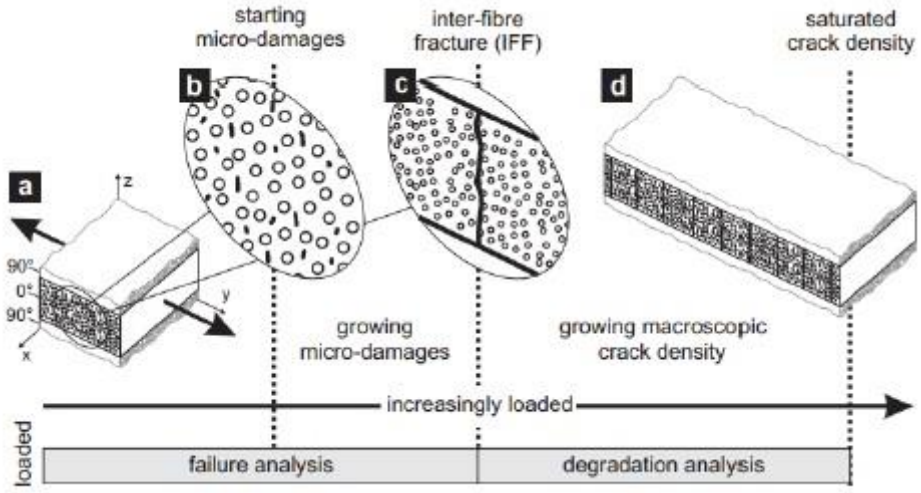

Figure 16. Appearance of cracking and subsequent degradation [21]

3.2.1 Continuum damage mechanics (CDM)

As has been said previously, after predicting the onset of the damage it is necessary to predict its evolution. Therefore, the “Failure criteria” method is often combined with the CDM models, which according to [22] *“…homogenize the damage by reducing the stiffness using a second or fourth order phenomenological damage tensor by fitting the evolution of damage variables with an evolution equation”*. However, this methodology has some limitations as: (i) the requirement of parameters that are difficult to determine experimentally, (ii) their mesh dependence and (iii) the difficulty to describe the local effects of the stress redistribution of the damage zone [22, 23]. Thus, a more useful alternative to these methodologies is the discrete damage mechanics model (DDM) presented in the following section.

3.2.2 Discrete Damage Mechanics Model (DDM)

With this model it is possible to predict with accuracy the strain that cause the appearance of the first crack, the evolution of the crack density as a function of applied strain and how the degradation of the mechanical properties of the cracked lamina affects to the redistribution of the stresses in the laminate [22]. As it was mentioned by Barbero [24], *"…the formulation uses a representative volume element (RVE) enclosed by the mid-surface and the top-surface of the laminate denoted with t (*Figure 17*), the surface of two consecutive cracks, and a unit length parallel to the cracks. The length of the RVE is equal to 2l (distance between two adjacent cracks), and is related to the crack density that is the inverse of this distance (λ=1/2l)"*.

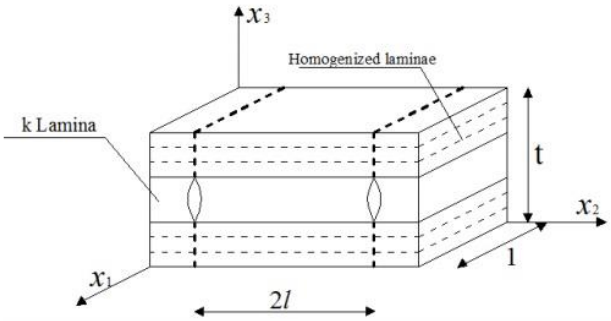

Figure 17. Representative volume element RVE [24]

Moreover, Barbero [24] also described that *"…the cracks occupy the entire thickness of the lamina. Three coordinate systems are used: the lamina coordinate system (1,2,3;*Figure 18*) with the 1-axis along the fiber direction of each lamina, the laminate coordinate system (X,Y,Z;* Figure 18*) where loads and boundary conditions are applied, and the cracking lamina coordinate system (x_1,x_2,x_3;* Figure 17*) coinciding with the lamina coordinate system of the current cracking lamina k*".

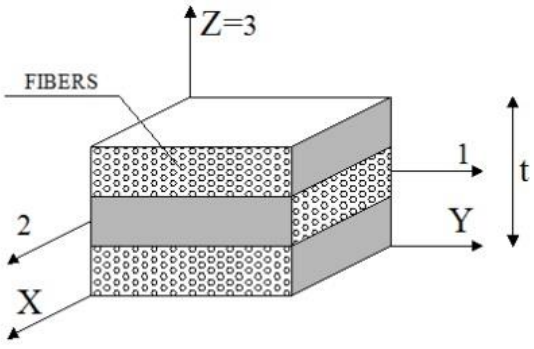

Figure 18. Coordinate systems used for the RVE [24]

In DDM, fracture mechanics is used instead of strength criteria. Some basic principles of fracture mechanics will be presented now in order to have a small notion about the evolution of this field and

its relation and its possible application in this DDM. Griffith [25] contributed in the onset of the fracture mechanics studies for metals with his analysis of crack stability based on energy equilibrium. When a crack is in equilibrium, the increase of surface energy (S) must be equal to the decrease of strain energy (U) due to crack extension (equation 22) [20]

$$\frac{\partial U}{\partial a} = \frac{\partial S}{\partial a} \tag{22}$$

where a is the crack length and $\frac{\partial U}{\partial a}$ is the strain-energy-release rate (the crack-extension force) . This Griffith's theory was extended by Irwin [26] to elastic-plastic materials and explaining the three kinematically admissible crack-extension modes: (I) Opening mode, (II) Forward-Shear mode, (III) Parallel-Shear mode; which are shown in Figure 19.

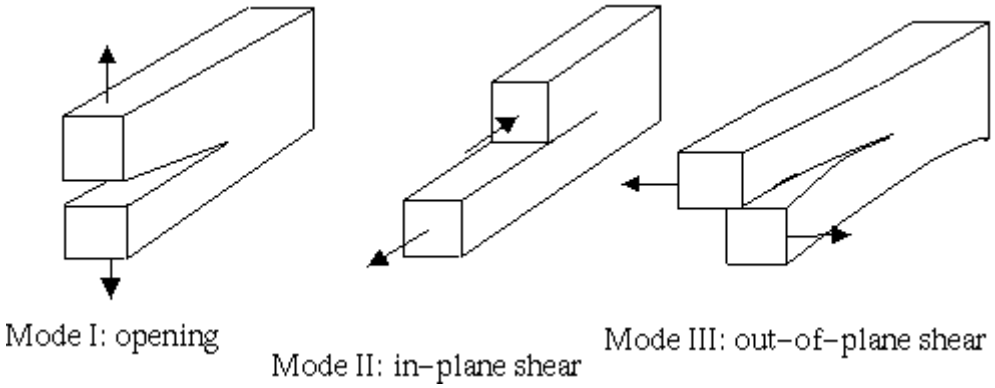

Figure 19. Crack-extension modes

Irwin [26] used the strain-energy release rate in terms of stresses around a crack tip. He considered a crack under two different stresses relative to the crack: a plane stress loading of (σ^{∞}) and a skew-symmetric stress (τ^{∞}). The superscript "$^{\infty}$" means that the stresses are applied far from the crack tip (an "infinite distance") as it is shown in Figure 20.

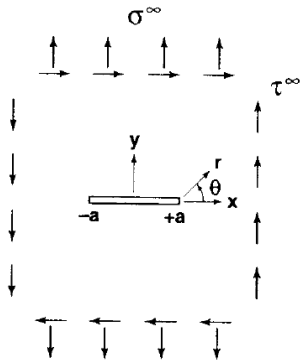

Figure 20. Cracked plate with symmetric and skew-symmetric stresses at infinity [20]

Subsequently, the symmetric and skew-symmetric stress intensity factors, k_1 and k_2, are associated with the opening mode of crack extension and with the forward-shear mode respectively:

$$k_1 = \sigma^{\infty}\sqrt{a} \tag{23}$$

$$k_2 = \tau^{\infty}\sqrt{a} \tag{24}$$

In contrast to what it happened with the metals, for composite materials it is impossible to generalize the features of the surfaces of fracture, as well as the trajectories of the cracks, since they depend on the multiple types of fibre reinforcements and matrix. In addition, for the same *"composite"*, the fracture features change according the nature of the fiber-matrix interface. The anisotropy and heterogeneity due to the fibers, the matrix and the different orientations, are the principal sources of problems.

This way, it is possible to distinguish between the cases in which, after the fracture, rests of the matrix remain attached to the fibers and those in which there are no waste. First situation appears when there is a strong union between the matrix and the reinforcement, being named as *cohesive fracture*. While the second case belongs to composites with a weak fiber-matrix interface, receiving the qualifying of *adhesive fracture*. So the fracture surfaces of the composite materials give an indication of the type of mechanism of reinforcement that acted during the fracture process.

Wu [16] proposed that the intensities of the stresses σ_x, σ_y and τ_{xy} are controlled also by functions of the anisotropic material properties and the orientations of the crack relative to the principal material directions apart of the parameters: $\sigma^{\infty}\sqrt{a}$ and $\tau^{\infty}\sqrt{a}$ [20].

More recent studies, discuss fracture mechanics through the micromechanics, as proposed by Tetelman [14] and Corten [27], while other authors extend the concepts of fracture mechanics to laminates.

As it has been said previously, in DDM, fracture mechanics is used instead of strength criteria. The material properties that governs the damage evolution in a laminate are the critical values of the energy release rates in modes I and II (G_{Ic} and G_{IIc}). They were successfully used for predicting damage initiation, damage evolution, stress redistribution and laminate ultimate strength [28, 29].

Damage initiation

Damage initiation criteria is based on the results given by the function g(λ,ε):

$$g\ (\lambda, \varepsilon) = \frac{G_I(\lambda,\varepsilon)}{G_{Ic}\ (\lambda,\varepsilon)} + \frac{G_{II}(\lambda,\varepsilon)}{G_{IIc}(\lambda,\varepsilon)} - 1 \leq 0 \tag{25}$$

where $G_I(\lambda, \varepsilon)$ and $G_{II}(\lambda, \varepsilon)$ are the energy release rates (ERR) in modes I and I respectively. The energy release rate is the energy dissipated during fracture per unit of newly created surface area while the critical ERR is the fracture energy. So when the EER is higher or equal to the critical ERR, the failure will start.

A negative result of damage activation function g(λ,ε) means that there is no crack while function g(λ,ε) is equal to 0 means the crack will appear.

Damage evolution

After the appearing of the first crack, the next interests will focus on discovering how they evolve and when the following cracks are going to emerge. Barbero [30] proposed the same equation (equation 25) to predict the damage evolution. The state variable in this problem is the crack density. Every state variable has a thermodynamic force and, in this case (DDM), the thermodynamic quantity that drives the problem is the strain. This strain will be responsible for increasing the crack density, so if no more strain is applied, crack density will not grow. When crack initiation line in the Figure 21 is "touched" (i.e. intersected), the crack appears.

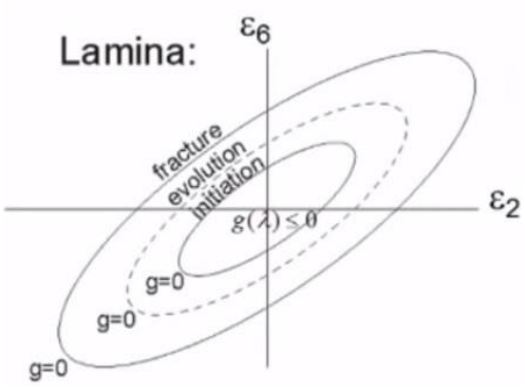

Figure 21. Evolution of the crack based on the strain

Additionally, it is needed an analytical calculation of the ERR's values G_I and G_{II} [24, 30]

$$G_I = -\frac{\partial U_I}{\partial A} \tag{26}$$

$$G_{II} = -\frac{\partial U_{II}}{\partial A} \tag{27}$$

where U_I and U_{II} are the strain energy for mode I and mode II, respectively, and A is the crack area.

The next step is to decide how much crack density to consider because the finite element program will drive the constitutive solver by strain. After calculating G_I and G_{II} and checking the damage activation function, if this function is greater than zero the crack density is calculated using a return mapping algorithm. Equation 28 provides the increment of crack density necessary to make g (λ,ε) exactly equal to zero and, in this way, be able to stop the damage evolution:

$$\Delta\lambda_k = -\frac{\partial g_k}{\partial \lambda_k} \qquad (k = 1, \dots, N) \tag{28}$$

Where subscript "k" refers to de damaged lamina [30] and N is the number of plies in the laminate. Figure 22 represents the algorithm followed by DDM. A "strain step", performed by the finite element package at a gauss point, comes through the plug-in to the laminate checking all the points shown in the algorithm diagram of Figure 22. At each load (strain) step, the strain on the laminate is increased and the laminae are checked for damage modes by evaluating the damage activation functions g≤0 of

all possible modes of damage, including: longitudinal tension, longitudinal compression, transverse tension and transverse compression. While the algorithm is checking the lamina failure, the new crack density (or its increment) and the stiffness reduction are computed if the activation function is greater than zero. After that, the stress redistribution of the laminate is calculated by the algorithm, which also checks for equilibrium and if it converges, then it gets out.

An important fact of this method is that the “strain step” goes into the laminate unlike many other models that follow the classical lamination theory where stain step goes into the lamina. This is the reason why the representative volume element in DDM is the laminate, because it is a necessity to know all the states of damage of all the laminas to calculate these quantities correctly [24, 28, 29].

Laminate ultimate strength

Once the crack onset, its evolution and the accumulate crack density is known, the stored damage in the composite will lead the laminate to the final failure.

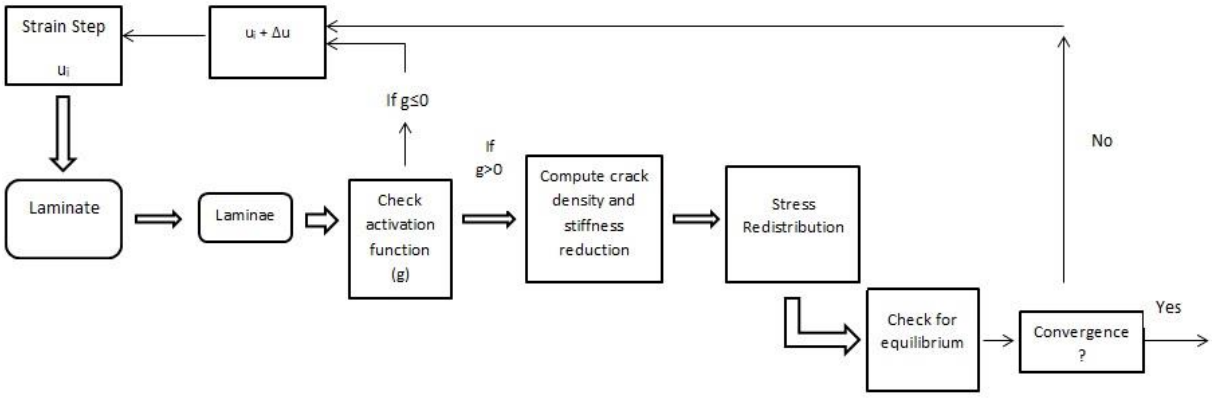

Figure 22. Algorithm of damage evolution for DDM

3.3 XFEM

The conventional methods for fracture modelling only allow the propagation of the crack along the elements that have been previously predefined. This implies a drawback with damage tolerance problems since it is necessary to define the area where the crack is going to generate and not always it is possible to carry out real experiments of the model to predict where this fact is going to happen. However, thanks to XFEM (eXtended Finite Element Method), used in a finite element software, the mesh is generated regardless of the existence and location of any cracks, so it is not necessary to create any special mesh. The XFEM was first introduced by Belytschko et Black in 1999 [31]. It is an extension of the conventional FEM based on the unity partition concept of Melenk and Babuska [32] that allows local enrichment functions easily embeddable into a finite element approximation. The original purpose of the XFEM method was the crack analysis, but soon covered other computational

applications including modelling fracture, void growth and phase change [33]. Through the XFEM method it is possible to study the onset and propagation of the crack in quasi-static problems. XFEM allows studying the crack growth along an arbitrary path without the need of remeshing the model and it is only available for 3D solid and 2D planar model (Figure 23). Crack can be defined by giving it an initial crack onset or alternatively, the finite element software allows the determination of its location during the analysis, based on the value of the maximum principal stresses calculated in the domain of the crack. Regardless of whether or not is defined the initial location of the crack, the finite element software starts it during the simulation process through the tracking of the regions that suffer principal stress higher than the maximum (allowable) values specified in traction-separation laws [31, 34, 35].

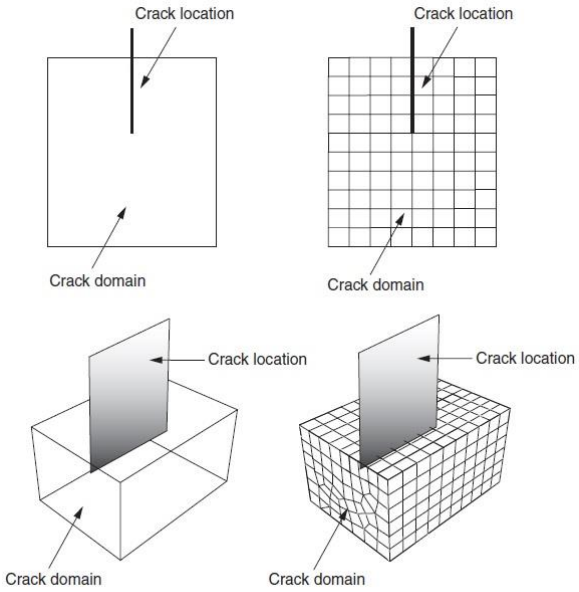

Figure 23. Defining a crack for XFEM [35]

A dynamic crack analysis carried out by XFEM involves two independent parts such as the crack tracking procedure and the dynamic crack propagation formulation. The method used by XFEM is the creation of “dummies” nodes as crack is spreading (Figure 24). The phantom nodes, which overlap with the originals, are introduced to represent the discontinuity of the cracked elements. When the element is intact, each ghost node is completely limited to the corresponding real node. When the element is cut through a crack, cracked element is divided into two parts. Each part consists of a combination of some of the real and phantom nodes depending on the orientation of the crack. Each ghost node and its corresponding real node are not already joined together and can be separated. This system of remeshing is very effective because you can perform more complex crack propagation models since the user does not have to intervene in each analysis increment.

.

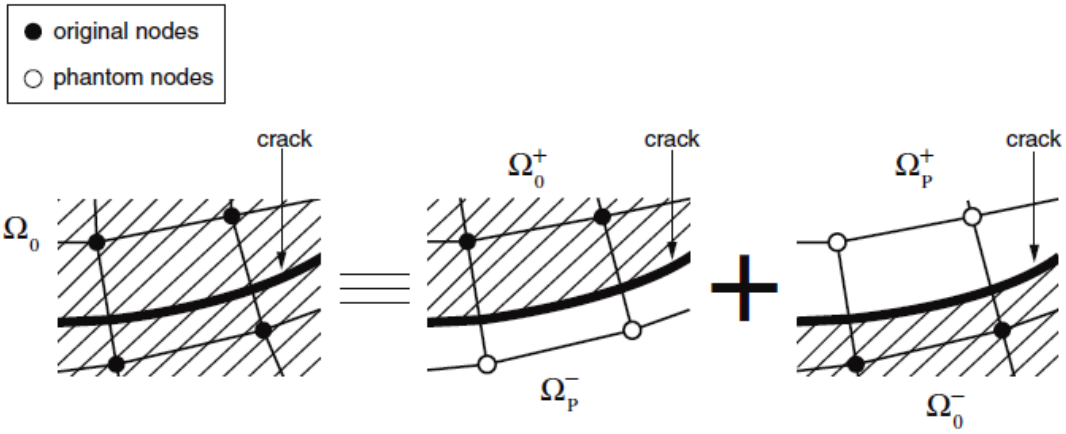

Figure 24. Phantom and real nodes near the crack [34]

In case of FE software Abaqus, there is a module that is able to determine the carrying capacity of a cracked structure as well as providing their respective results for further treatment, thanks to STATUSXFEM and PHILSM outputs. Those nodes responsible for this are the phantom nodes (dummies) that have been created at the time the crack was extending, the method of integration that takes place in these nodes cancels the percolation of stress through that area and distributes it to adjacent nodes. For the correct identification of the output variables, use of the options that have been mentioned before must be made: (i) PHILSM (ϕ), which describes the face of fracture, (ii) PSILSM (ψ), which describes the forehead of initial fracture, and (iii) STATUSXFEM, which specifies whether the item is fully, partially or not cracked [31, 33, 34]. The level set method used in XFEM is a popular numerical technique for representing surfaces in interface tracking problems, which means that it locates and tracks the motion of the crack.

The functions ϕ and ψ are used to completely describe the crack. The first one describes the crack surface (ϕ) while the second one is constructed so that the intersection of two level sets gives the crack front (ψ) (Figure 25). According to Zhen-Zhong Du [34]: *"…the nodal value of the function ϕ is the signed distance of the node from the crack face with a positive value on one side of the crack face and negative on the other. The nodal value of the function ψ is the signed distance of the node from an almost-orthogonal surface passing through the crack front with a zero value on this surface and a negative value on the side towards the crack"* [34] (Figure 25).

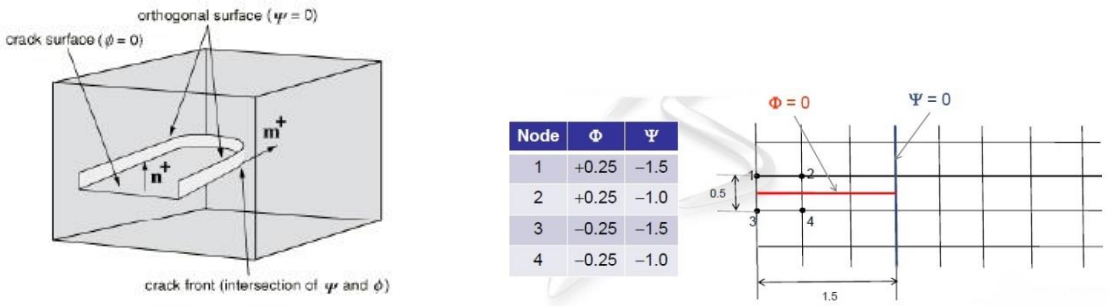

Figure 25. Level set method for locating crack [34]

Conventional FEM methods use a piecewise polynomial function that is extended in XFEM with two more extra terms (Equation 29) [34]:

- Heaviside function to represent displacement jump across crack face [$H(x)a_I$; *with I∈ N_T*], where *H(x)* is the Heaviside distribution, a_I is the nodal enrichment degrees of freedom (DOF) vector and N_T the nodes belonging to elements cut by crack.
- Crack tip asymptotic function to model singularity [$\Sigma_1^4 F_\alpha(x) b_I^\alpha$; with *I∈ N_A*], where F_α are the crack tip asymptotic functions and b_I^α the nodal DOF vector.

$$u(x) = \Sigma_{I \epsilon N_T} N_I(x)[u_I + H(x)a_I + \Sigma_1^4 F_\alpha(x) b_I^\alpha] \quad (29)$$

where $u(x)$ is the displacement vector, N_I are the shape functions and u_I are the nodal displacement vectors.

Two different views are offered by the FE software Abaqus for the study of the initiation and propagation of the cracks using XFEM: (i) “Traction-separation cohesive behavior” and (ii) “Linear elastic fracture mechanics”. This second method uses the “Virtual crack closure technique” to calculate the energy release speed on the edge of the crack. Traction-separation cohesive behavior is used in Abaqus to simulate the onset and the propagation of the crack. It may be employed for brittle and ductile fracture, simulating the break in a random way or through a given solution, since is not linked to meshing elements. Linear elastic fracture mechanics is an alternative approach being more appropriated to the problems in which the propagation of brittle cracks happens, considering only the leap through the cracked elements. Fracture here must propagate through the entire item, avoiding the need for modelling the singularity of stresses [34].

Therefore, XFEM is capable of analyzing non-linear materials and complex geometries, improving the convergence rates in stationary cracks and defining the onset of the crack with meshing independent of the crack. However, it has some limitations: (i) fatigue crack growth phenomenon cannot be modeled; (ii) a crack cannot turn more than 90 degrees within an element; (iii) crack branching is not allowed; (iv) only single or non-interacting cracks can be contained in the domain; (v) parallel processing of elements is not allowed.

Chapter 4

SELECTED STUDIES ON DAMAGE OF COMPOSITES

With the increasing rate in the use of composites in the aerospace industry, there have been many studies on the characterization of damage and failure in composite materials during the past years. Different numerical techniques and computational methods of analysis have been used to predict and locate the damage experienced by a given composite. Apart from other specific software, the FE code Abaqus is the software more commonly employed to carry out these studies. The purpose of this chapter is not to give a comprehensive review of available studies but rather to present some investigations on damage of composites carried out in Abaqus framework. Therefore, the most significant results of three selected works (FE models) related with damage mechanics, crack spreading and progressive failure of composite materials are presented in this chapter.

4.1 Huang's Model

Within the study of the failure of composite laminated structures, Huang [36] proposed a nonlinear constitutive law for degradation material properties. In order to describe the laminate nonlinear constitutive relationship due to the matrix inelastic deformation, the author makes use of the Bridging Model theory [37]. This theory was incorporated into the Abaqus through programming a user subroutine UGENS for analyzing the nonlinear response and ultimate strength of composite laminates. This subroutine "helps" Abaqus to define the elementary stiffness matrix in FE solution, to update the internal stresses of all the plies of the element and to check how many plies have failed at this load increment.

Two different studies are carried out in [36], a "laminate under bending" and "laminates subjected to in-plane loads".

For the "laminate under bending" case, a laminate made of carbon fibers and epoxy matrix is used (Figure 26). This laminate is a 12-ply laminated beam subjected to 3-point bending with a stacking sequence of $[0/\pm45/0/90/0]_s$. After applying a distributed load in the midspan of the beam along width direction, some different analyses are carried out for different load increments (Figure 27), different mesh sizes (Figure 28) and different Abaqus element types (S3R and S4R) (Figure 29).

Figure 27 shows that the choice of a load increment of 10N or a load increment of 2N does not change the accuracy. However, when using a load increment of 2N, the solution time was increased, from 6 minutes (when using 10N) to 27 minutes (when using 2N). Likewise, Figure 28 shows that even the coarsest mesh size gave good results, while Figure 29 indicates the validity of using S4R and S3R Abaqus elements with the developed UGENS routine.

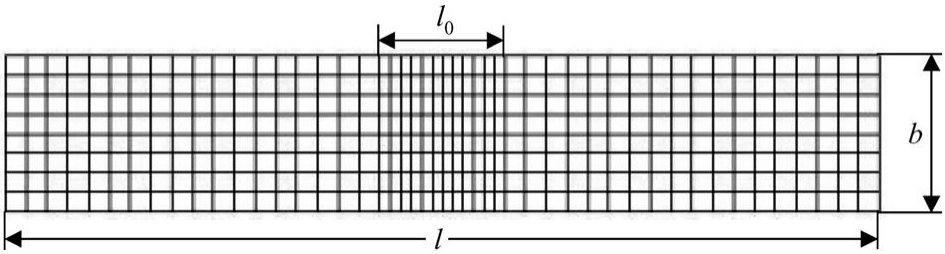

Figure 26. Schematic meshes of a laminated beam subjected to 3-point bending [36]

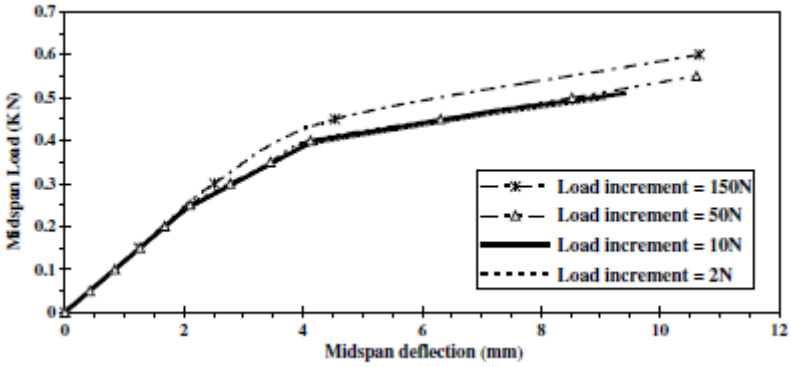

Figure 27. Load-midspan deflection curves comparison for different load increments [36]

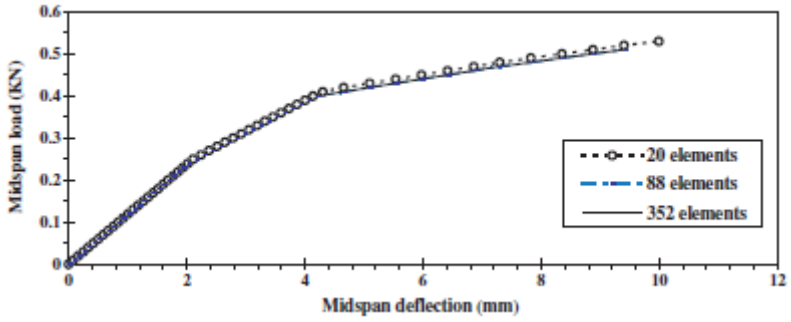

Figure 28. Midspan load- deflection curves comparison for different mesh numbers [36]

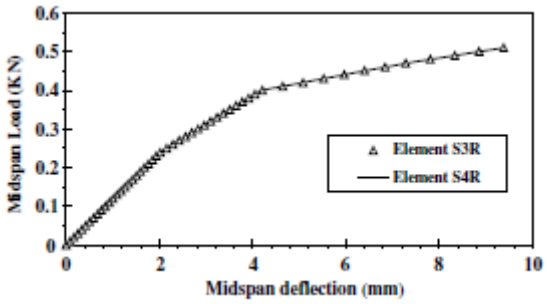

Figure 29. Midspan load-deflection curves comparison for different Abaqus element types [36]

These load-displacement curves have been compared with experimental results in order to prove the validation of the used model. In Figure 30 the results of different analyses to determine the first, second and third ply failure, respectively, can be seen.

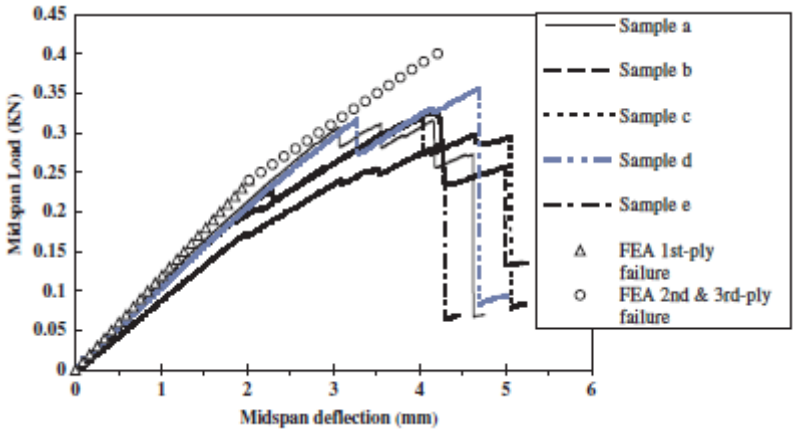

Figure 30. Comparison between FEA and experiment data [36]

For the “laminates subjected to in-plane loads” case, four different kinds of laminates are studied. These laminates are subjected to uni or bi axial in-plane loads up to ultimate failure. After comparing the different results obtained with experiment, FEA and theoretical analysis, good correlations were found for all of the four laminates. Therefore, the nonlinear and ultimate strength calculated using Abaqus agreed reasonably with available experimental data.

4.2 Chen et al. Model

Within the framework of the progressive failure analysis studies, it was possible to find the work by Chen et al. [38], where the application of the s-version finite-element method (SFEM) in the failure analysis of open-hole composite plates was studied by using Abaqus. In order to carry out these studies with a high computational efficiency, it was necessary to include into the procedure the FORTRAN scientific programming language and the PARDISO package, which solve highly complicated and sparse nonlinear equations.

For a rectangular plate with a hole (Figure 31), and the following stacking sequence $[45/-45/90/45/-45/45/-45/0/45/-45]_S$ for a T700/epoxy prepeg composite material, precision and efficiency of the S-FEM are compared with the traditional FEM results.

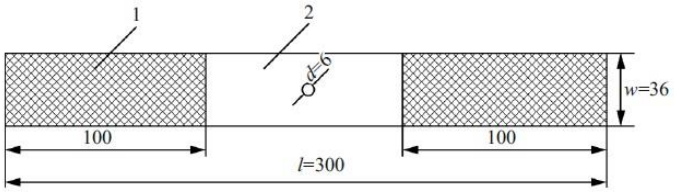

Figure 31. Test specimen: 1 — griping region and 2 — gage section. Dimension in mm [38]

When using SFEM (which is a superposition finite element method) in the open-hole problems and according to Chen et al. [38], *"…the structure is discretized by a global finite-element mesh as a whole, and the vicinity of the hole is discretized by a local mesh"* so *"…the global and local regions are denoted as Ω^G and Ω^L "*. Figure 32 shows these ideas about how the finer mesh is superimposed on the global one.

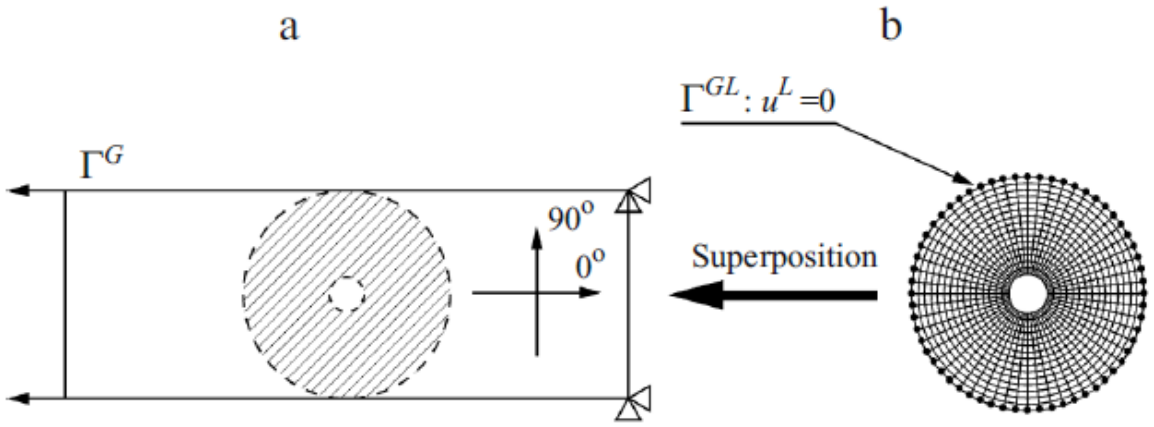

Figure 32. Open hole problem using SFEM: (a) global Ω^G and (b) local Ω^L meshes [38]

During the progressive failure analysis, the Hashin method was utilized to estimate the stresses at any material point of a ply (Gauss point). The algorithm used to carry out the failure analysis of these composite laminates with the SFEM is reflected in Figure 33.

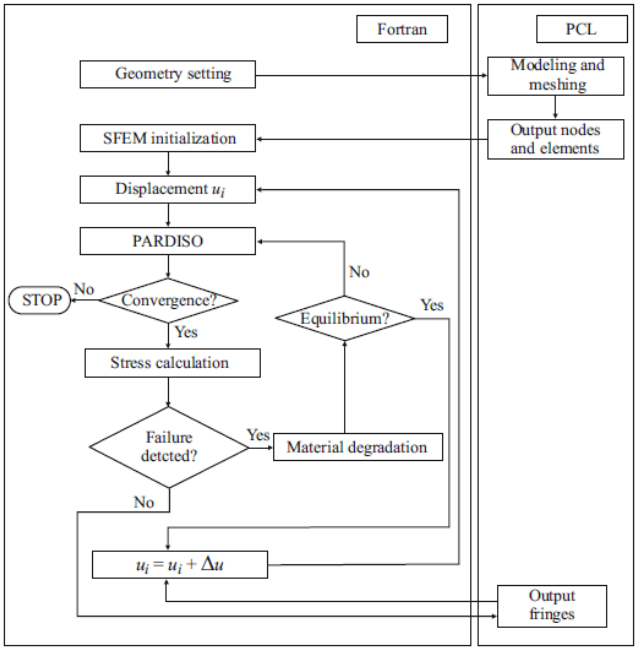

Figure 33. Algorithm for a failure analysis of composite laminates by using SFEM [38]

The selection of the geometry of the local region was a critical issue. There was a necessity of setting the diameter of the outer circle equal to the width of the plate. So in this case, the critical region could be cover to the maximum extent causing the disappearance of the transition region in the meshing, which implies a clear loss of elements and nodes in using SFEM (Table 5).

Table 5. Differences in number of elements and nodes between two finite-element models

Number	ABAQUS	SFEM		
		Global mesh	Local mesh	Sum
Number of nodes	21420	4	960	964
Number of elements	19510	1	900	901

After carrying out some experimental, SFEM and Abaqus FEM analyses, it can be concluded that the load-displacement curves predicted by the present method were in good agreement with the experiment results and Abaqus (Figure 34).

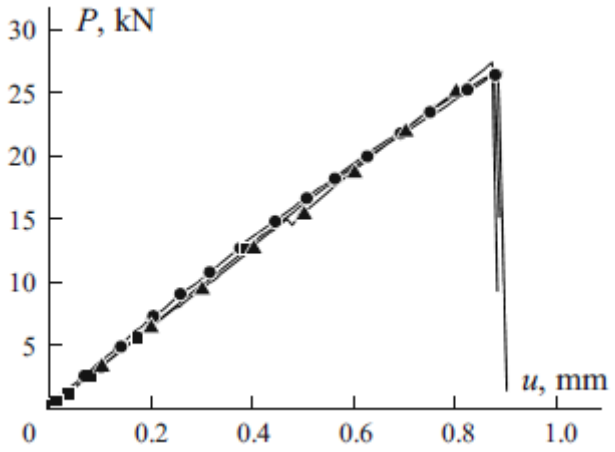

Figure 34. Load-displacement curves obtained by using EXPERIEMENT (■), ABAQUS (•) and SFEM (▲) [38]

After analyzing mesh and convergence dependence, the study concluded that the mesh dependence is revealed to be minimum and the convergence problem is also not of great concern. So this SFEM procedure describes reasonably well the damage process of the analyzed composite material with (i) mesh independence, (ii) reduction of modeling difficulties and (iii) accuracy comparable with that provided by the conventional FEM.

4.3 Moure et al. Model

Another interesting study is the one carried out by Moure et al. [22]. The main objective of this study was to calculate the laminate stiffness reduction due to cracks in a composite plate, where the open holes are used as stress raisers. To study damage localization, the authors used the DDM methodology [30] extended to include fiber failure, by incorporating a simple fiber damage model that

required only single additional material property. The obtained results were classified as mesh independent.

The analyzed coupon is a square plate of *25 x 25 mm*^{2} with *1.25 mm* radius hole made from a glass/vinylester laminate (Fiberite/ HyE 9082Af) with the following stacking sequence: [0/90$_8$/0/90$_8$/0] Figure 35. The Table 6 shows the mechanical properties of the composite material used, where the values are given in [22, 28, 39].

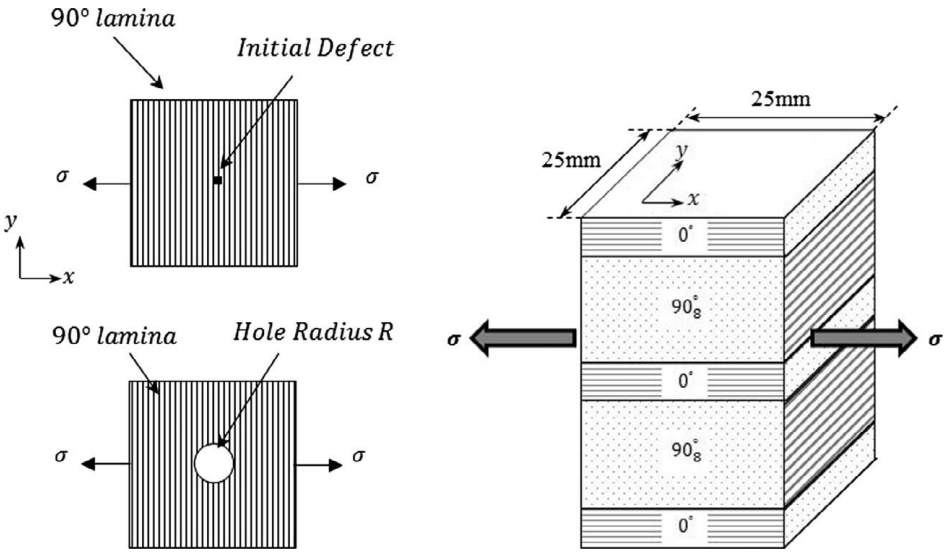

Figure 35. Distribution and orientation of the laminate plies [22]

Table 6. Mechanical properties of Fiberite/HyE 9082 Af

Property	**Units**	**Value**
Critical energy release rate, mode I, G_{IC}	(kJ/m^2)	0,254
Critical energy release rate, mode II, G_{IIC}	(kJ/m^2)	0,292
Tensile strength in the fiber direction F_{1t}	(MPa)	1020
Compressive strength in the fiber direction F_{1c}	(MPa)	620
Tensile strength in transversal direction F_{2t}	(MPa)	40
Compressive strength in transversal direction F_{2c}	(MPa)	140
Shear strength F_6	(MPa)	60
Transition thickness t_t	(mm)	0,6
Weibull modulus m	-	8,9
Young modulus in the fiber direction E_1	(MPa)	44700
Young modulus in transversal direction E_2	(MPa)	12700
In-plane shear modulus G_{12}	(MPa)	5800
In-plane Poisson's ratio v_{12}	-	0,297
Out-of-plane Poisson's ratio v_{23}	-	0,41
Lamina thickness t_k	(mm)	0,144

In order to analyze how loading, displacements and stresses affect the damage in the studied plate, a numerical model was implemented in Abaqus/Standard by programming a user subroutine UGENS. To carry out the plate meshing, rectangular elements (S8R) and triangular elements (STRI165) were used by the authors. After applying the appropriate boundary conditions and a horizontal displacement to simulate a uniaxial tensile load, the following results, shown in Figure 36, were obtained. This figure shows a linear behavior with an approximate stiffness of 50000 N/mm until about 0.49% strain, when it is possible to observe a reduction in modulus. This equilibrium configuration is when matrix damage extends over the entire plate and, soon after that, fiber damage begins to take place, leading to the failure of the laminate.

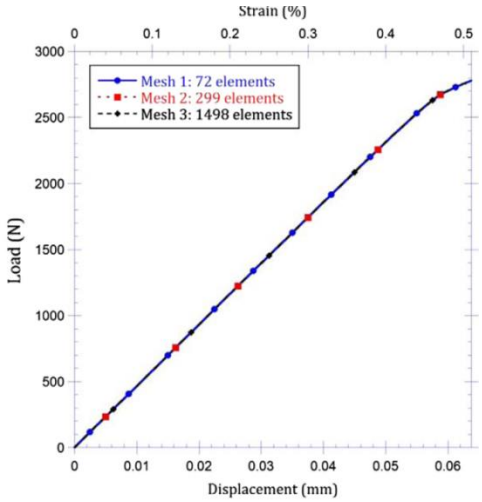

Figure 36. Load-displacement response in a plate with hole [22]

Making a comparison between this plate and another one with a larger hole (4.17 mm radius hole), it can be observed that the plate with the smaller hole is stiffer, so it experiences higher stress for the same applied strain, which means that the smaller one damages earlier (Figure 37).

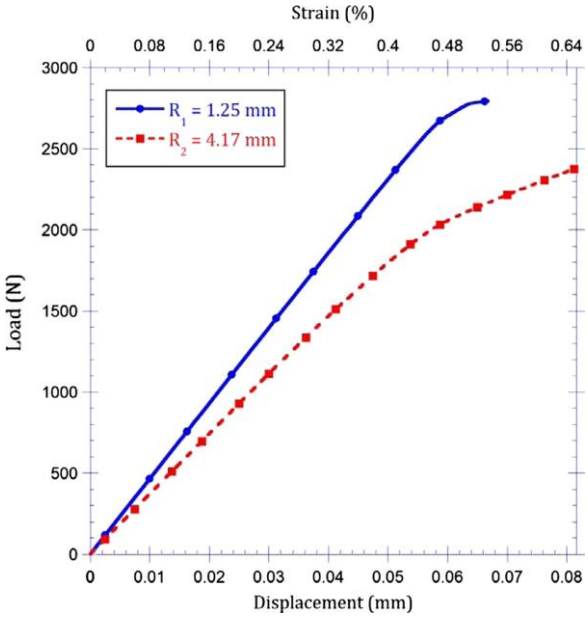

Figure 37. Load-displacement and load-strain for 2 hole radii: 1.25 mm and 4.17 mm [22]

Chapter 5

FE MODELLING OF DAMAGE IN COMPOSITES

In this chapter, a finite element model to investigate the damage and crack of fibre composite plates is shown. The characterization of the model will be first done, and then a validation of the model based on previous works will be carried out by comparing the obtained results with some available in the literature. For all of these purposes, the software Abaqus will be used, which will allow realizing the necessary analyses to reach the desired objectives of this work. Therefore, a preliminary elastic analysis will be done in order to evaluate the elastic stiffness of the plate and then the damage evolution will be studied throughout the use of both XFEM and Hashin damage criteria.

5.1 Characterization of the model

As has been said previously, composite materials present problems regarding their brittle behavior (interlaminar delamination and cracks), especially when they work under dynamic loading conditions, which may affect their strength and their integrity [33]. Thus, it is crucial to evaluate the structural integrity and the load carrying capacity of the structures made of composite materials. In practice, the composite structures employed may have complex shapes and be subjected to changeable load conditions, so a computer simulation is required to design engineering structures with composites and to perceive the stiffness and strength of the laminated composites [36].

One of the most successful programs to achieve these goals is the FE software Abaqus [35], which is a very useful tool. Abaqus has a wide library of finite elements that allows virtual modelling of any geometry, as well as its wide list of models that simulate the behavior of a large amount of materials, which is very useful in many areas of engineering. Among several modules, two different modules were used:

- Abaqus/CAE: an application used for modelling and analyzing mechanical components and assembly of parts. It is also possible to post-process the program results with the Abaqus/Viewer.
- Abaqus/Standard: the module for general analysis, which employs the traditional system of implicit integration.

In order to validate and calibrate the developed model, the model presented in this work is the same as the one analyzed by Moure et al. [22] – see previous chapter. This way, a model was developed within the framework of XFEM and Hashin criterion.

The chosen design is a fiberglass laminate with a square shape and a center hole. Plates with holes are very common in aerospace industry in order to make mechanical joints between different laminates that make up the parts of an aircraft. However the mechanical joints tend to present problems in form of cracks due to high stresses concentrations around the hole and to the reduction of the strength. There are several failure modes as it is represented in Figure 38.

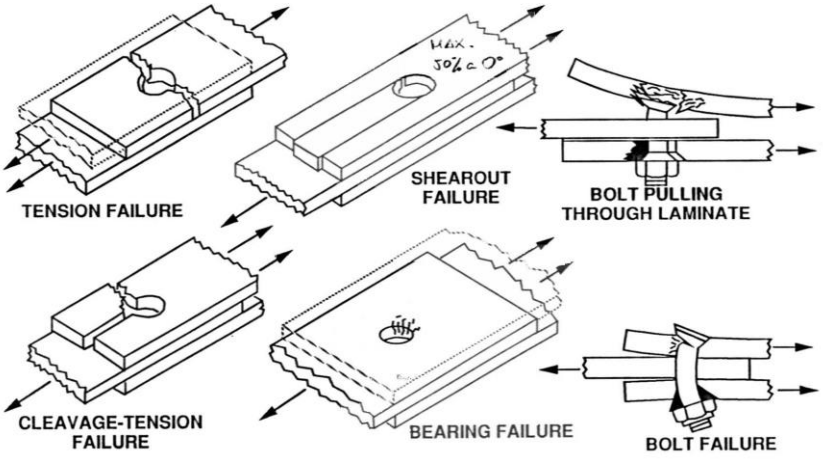

Figure 38. Failure modes in mechanical joints of laminates [12]

The specimen is made of a glass/vinylester laminate (Fiberite/HyE 9082Af) consisting of 19 plies with the following stacking sequence: $[0/90_8/0/90_8/0]$. Where subindex “8” means that there are 8 plies in that direction. Likewise, the square plate (25x25 mm) has a center hole (1.25 mm radius) that goes through the entire thickness of the plate. Because each ply has a thickness of 0.144 mm, it can be concluded that the plate has a thickness of 2.736 mm. In Figure 39, it can be observed the different views of the square plate and the orientations of the (x, y, z) axes.

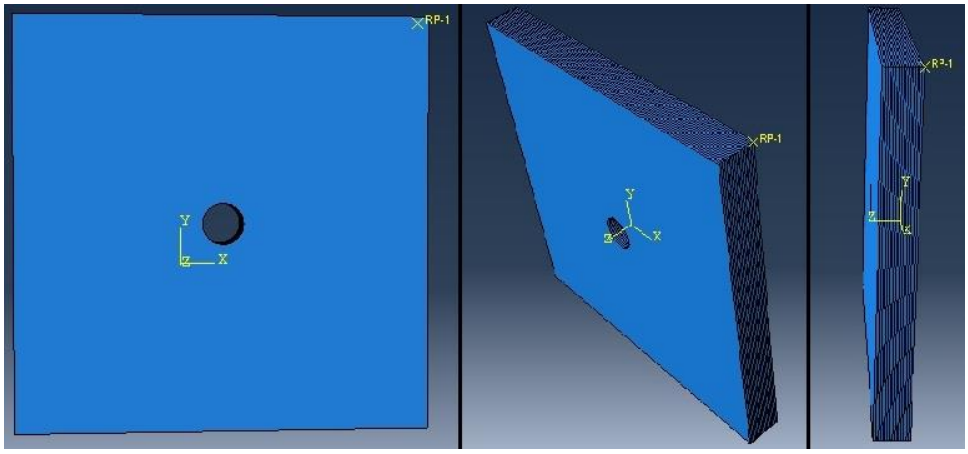

Figure 39. Different views of the square plate

In order to define the geometry and the composite material compatible with the XFEM method, a solid deformable part is created with Abaqus and after that the plate is partitioned along its thickness in 19

sheets. In order to simulate the different orientations of the plies that make up the composite plate, each one of these 19 partitions will be assigned a different section with different material properties.

Once the geometry and shape of the plate has been defined, it is possible to mesh the geometry to proceed to the calculation. It is important to bear in mind that XFEM analyses do not have mesh dependence while the Hashin analyses do. For the purpose of XFEM analyses, solid (3D) finite elements with label C3D8R were chosen. This finite element is a general purpose linear brick element of 8 nodes, with reduced integration (1 integration point) and hourglass control. For the purpose of Hashin analyses, shell finite elements SC8R were chosen. This type of element is a general purpose element of 8 nodes belonging to the continuum shell elements family with reduced integration and hourglass control. Some of the reasons for using these continuum shell elements for the Hashin analyses reside in that they support linear and non-linear behavior, they present more accurate contact modeling than conventional shells by taking into account the two-sided contact and thickness changes and the most important one is that they capture more accurately the through-thickness response for composite laminates structures. These types of finite elements were chosen because XFEM does not run for shell elements and Hashin damage criterion is not implemented for solid elements. Likewise the meshing density is also defined in this step, taking a value of 0.80 mm^{-1} for XFEM and 0.84 mm^{-1} for Hashin-based method. The problem size includes 11420 elements and a total number of variables in the model of 77526 for XFEM and 869 elements and 4316 variables for Hashin-based method, for the analyzed stacking sequence $[0/90_8/0/90_8/0]$.

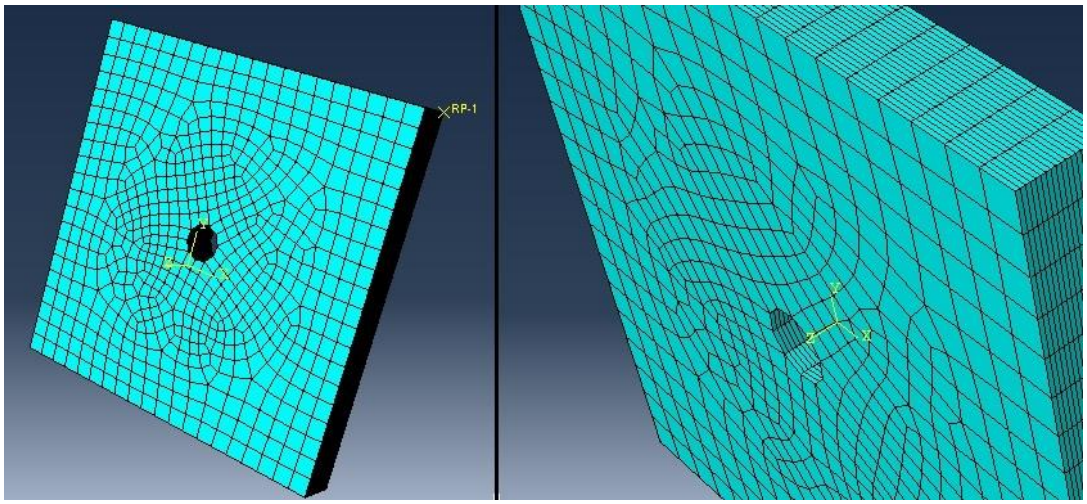

Figure 40. Final meshing of the square plate

To be able to define correctly the boundary conditions and the applied loads on the analyzed structure, thus mimicking the experiments by Moure et al. [22], it is necessary to create a rigid surface on the side of the plate where the load/displacement is applied – see Figure 41. As is shown in Figure 41, the rigid body constraint is a sequence of elements and nodes whose motion is controlled by the motion of a single reference point (which is set on the top right corner of the right side of the square plate, RP_1). Therefore the relative positions of the regions that are part of the rigid body remain constant throughout the analysis.

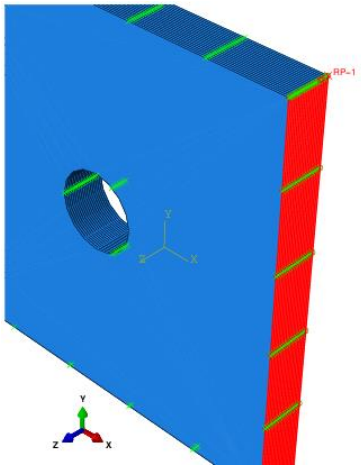

Figure 41. Rigid surface of the analyzed plate

After defining the rigid body, the boundary conditions are imposed over the square plate. These boundary conditions are applied over the left and the right sides, as it appears in red color in Figure 42. In order to fix the plate, all displacements and rotations are restricted on its left side while on the right side the displacements in Y and Z axes directions are the ones fixed. These boundary conditions are applied in the initial step while a displacement in X axis direction is used to simulate a progressive tensile loading in the next step of the analysis. Figure 43 shows these applied displacements which are imposed on the four corners of the rigid surface previously mentioned.

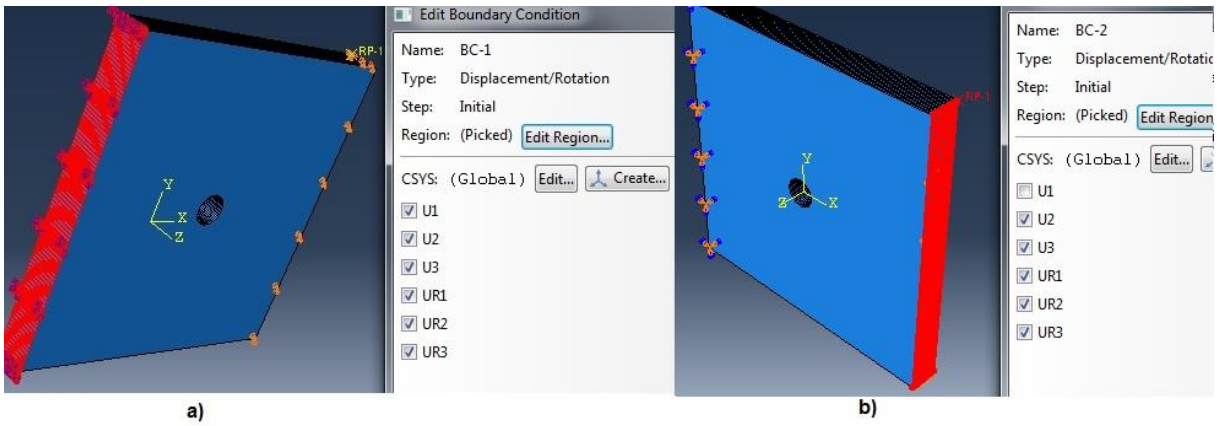

Figure 42. Boundary conditions on the left (a) and on the right side (b) of the square plate

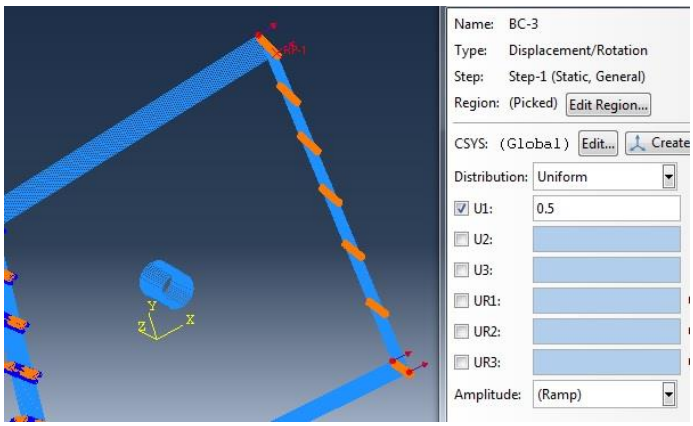

Figure 43. Applied displacements on the four corners of the rigid body

It is important to notice that when carrying out the analyses, come convergence problems appears. These problems are solved by modifying some parameters as the number of cutbacks, the viscosity coefficients and the initial increment size.

The elastic properties for the orthotropic material (Fiberite/HyE 9082 Af) analyzed during this work are described below (Equations 30-47). It is necessary to bear in mind that directions 1 and 2 correspond to the 1 and 2 axes previously defined in Figure 18.

This way and taking into account all the previous considerations, the following results are obtained for the 0^o plies:

$$D_{1111} = E_1(1 - \nu_{23}\nu_{32})\psi = 50907{,}5\ MPa \quad (30)$$

$$D_{2222} = E_2(1 - \nu_{13}\nu_{31})\psi = 16556{,}6\ MPa \quad (31)$$

$$D_{3333} = E_3(1 - \nu_{12}\nu_{21})\psi = 16950\ MPa \quad (32)$$

$$D_{1122} = E_1(\nu_{21} + \nu_{31}\nu_{23})\psi = 8091{,}3\ MPa \quad (33)$$

$$D_{1133} = E_1(\nu_{31} + \nu_{21}\nu_{32})\psi = 9243{,}1\ MPa \quad (34)$$

$$D_{2233} = E_2(\nu_{32} + \nu_{12}\nu_{31})\psi = 7729{,}4\ MPa \quad (35)$$

$$D_{1212} = G_{12} = 5800\ MPa \quad (36)$$

$$D_{1313} = G_{13} = 5800\ MPa \quad (37)$$

$$D_{2323} = G_{23} = 4503{,}55\ MPa \quad (38)$$

Where $\psi = 1/(1 - \nu_{12}\nu_{21} - \nu_{23}\nu_{32} - \nu_{13}\nu_{31} - 2\nu_{21}\nu_{32}\nu_{13})$

In case of 90^o plies, the following elastic properties were obtained:

$$D_{1111} = 16556.6\ MPa \quad (39)$$

$$D_{2222} = 50907.5\ MPa \quad (40)$$

$$D_{3333} = 16950\ MPa \quad (41)$$

$$D_{1122} = 8091.3\ MPa \quad (42)$$

$$D_{1133} = 7729.4\ MPa \quad (43)$$

$$D_{2233} = 9243.1\ MPa \quad (44)$$

$$D_{1212} = 5800\ MPa \quad (45)$$

$$D_{1313} = 4503.6\ MPa \quad (46)$$

$$D_{2323} = 5800\ MPa \quad (47)$$

Likewise, there is a need to define a set of parameters required by Abaqus in order to perform the analysis using the XFEM and Hashin damage methods. Therefore, it will be necessary to provide certain variables to input in Abaqus software, such as the fracture energy, the maximum principal stress and the different strength values. These values were taken from Moure et al. [22], except when missing (which is the case of the values of the critical energy release rates for the four Hashin damage modes). In this case, average values were taken from the literature. As it was carried out previously, these values should be differentiated between the 0^o and 90^o plies. All these parameters are illustrated in Tables 7 and 8 for the different damage methods and the different plies orientation.

Table 7. Main parameters required by XFEM

Property	**Fibre Direction**	
	0°	**90°**
Maximum Principal Stress [MPa]	1020	40
Fracture Energy [mJ/mm^2]	0.254	0.254

Table 8. Main parameters required by Hashin

Property	**Fibre Direction**	
	0°	**90°**
Longitudinal Tensile Strength [MPa]	1020	40
Longitudinal Compressive Strength [MPa]	620	140
Transverse Tensile Strength [MPa]	40	1020
Transverse Compressive Strentgh [MPa]	140	620
Longitudinal Shear Strength [MPa]	60	60
Transverse Shear Strength [MPa]	60	60
Fracture energy [MPa]	0.254	0.254

After the definition of all of these values, it was possible to proceed with the numerical analysis. Two different types of analysis, including a XFEM and Hashin-based analysis, will be carry out in order to determine the elastic stiffness of the studied plate and then its strength, thus comparing the results obtained from XFEM and Hashin-based analysis.

5.2 Validation for stiffness

In order to validate the numerical model developed in the current work, the results were compared with the experimental test results presented by Moure et al. [22]. This way, these results obtained in [22] will be used for making a stiffness validation of the XFEM and Hashin-based analyses performed in the current work. Figure 44 shows the variation of tensile force with the imposed displacements. It can be concluded that the curve corresponding to XFEM model (red line) matches almost perfectly the experimental test curve (green curve). This means that the elastic stiffness given by the XFEM model is accurate. Regarding the curve provided by Hashin-based analysis (blue curve), it can be concluded that it follow well the XFEM curve for low to moderate load level, but for moderate to high loading it tends to diverge slightly, being the behavior more stiff than the experimental test. Generally speaking, Figure 44

shows a good agreement in the behavior of the three cases. The small differences arise due to different finite elements used, solid elements in case of XFEM and shell in case of Hashin-based analysis.

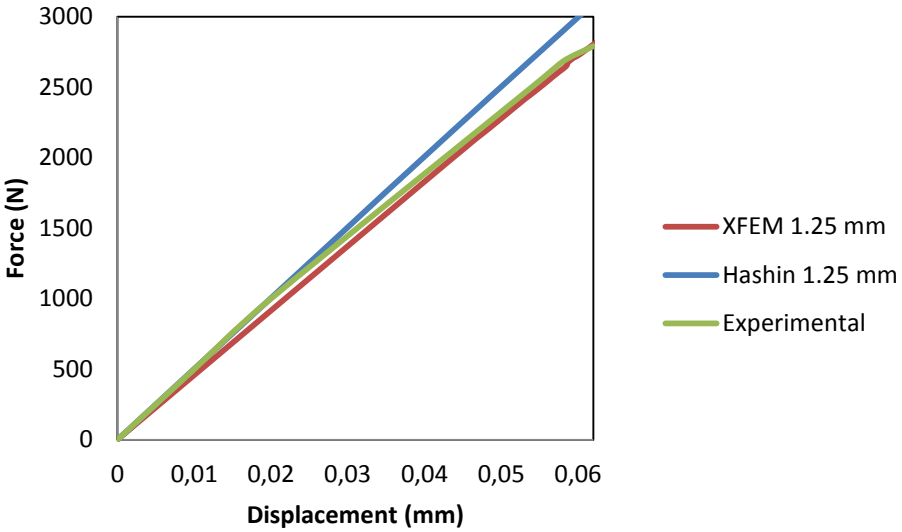

Figure 44. Comparison for the model validation for stiffness

Below, the damage and stresses evolution is presented through the progressive applied displacement. For this purpose, five F-d points have been taken as reference: elastic zone, first failure, mid-point before final failure, final failure and point after failure. Table 9 and Table 10 show all of these values above mentioned. It can be seen that a maximum force of 4470 N was obtained for the Hashin-based analysis while a maximum force of 7523,9 N was obtained in case of XFEM analysis. Unlike the stiffness, a very high difference exists in strength of the plate. However, if loads at first failure are compared, the force values (3591,14 for Hashin and 3319,54 for XFEM) as well as the displacements (0,0749 for Hashin and 0,0767 for XFEM) are in good agreement.

Table 9. Load-displacement (F-d) equilibrium points obtained from Hashin-based analysis

Force [N]	Displacement [mm]	Abaqus increment
2184	0,044	7
3591	0,075	16
3738	0,165	552
F_{max}=4470	0,217	872
1084	0,437	1211

Table 10. Load-displacement (F-d) equilibrium points obtained from XFEM analysis

Force [N]	Displacement [mm]	Abaqus increment
1150	0,025	9
3319	0,077	99
6040	0,150	246
F_{max}= 7524	0,191	289
5097	0,191	364

5.3 Parametric studies

After having validated the model, parametric studies will be shown. Namely, two type of studies will be presented, one related with the different layer configurations and another with different hole radii. Four different types of laminate configurations will be analyzed in order to carry out a parametric study which allows comparing the stiffness properties, the stresses and the forces and displacements when the crack onset appears. These four different stacking sequences are presented in Table 11 where the reference case is the one that appears in [22] and which was used previously to validate the XFEM and Hashin-based models. In all these studies, plates with three different hole radii were considered: one with a hole of 1.25 mm radius, a second one with a 2.50 mm radius hole and finally a third one with a hole of 5.0 mm radius. These studies will be presented separately for XFEM and Hashin-based models.

Table 11. Different stacking sequences

Case	Stacking sequence
Reference Case	$[0, 90_8, 0, 90_8, 0]$
I	$[90, 0_8, 90, 0_8, 90]$
II	$[90_8, 0, 0, 0, 90_8]$
III	$[0_8, 90, 90, 90, 0_8]$

5.3.1 XFEM results and discussion

When the XFEM analysis is carried out, it can be observed the crack onset and its growth through the entire laminate. For all the studied cases, it can be seen that the crack onset starts around the hole, where the highest stress concentration occurs. When the reference case is analyzed, this failure firstly appears in the 90º plies which transmit the stresses to the central 0º ply resulting also in its failure. After that, the crack still grows perpendicularly to the 0º direction up to the top and the bottom edges. At this point the final failure occurs, taking place the breakage of the two external 0º plies around the central hole and the crack propagation perpendicular to the 0º direction.

Figure 45 and Figure 46 illustrate this mode I of fracture after applying a tensile load and the stresses evolution experienced by the composite plate for the “Reference case” configuration. Green zones show the maximum Von Mises stresses, which are always concentrated on the crack edge.

In order to show the material failure and crack propagation in a deeper (zoomed) way, Figure 47 illustrates the studied plate just before and after its final failure.

Once the crack path and the stresses distribution have been presented for the “Reference case”, it proceed to carry out a parametric study between the four different stacking sequences (Reference case, Case I, Case II, Case III) and the three different hole radii (1.25 mm, 2.50 mm, 5mm).

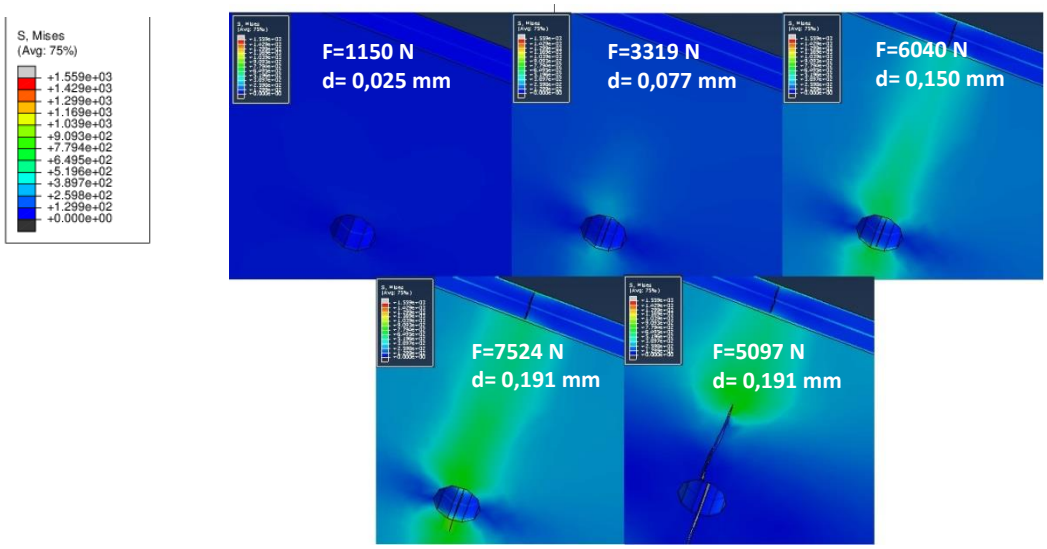

Figure 45. XFEM crack evolution for "Reference case"

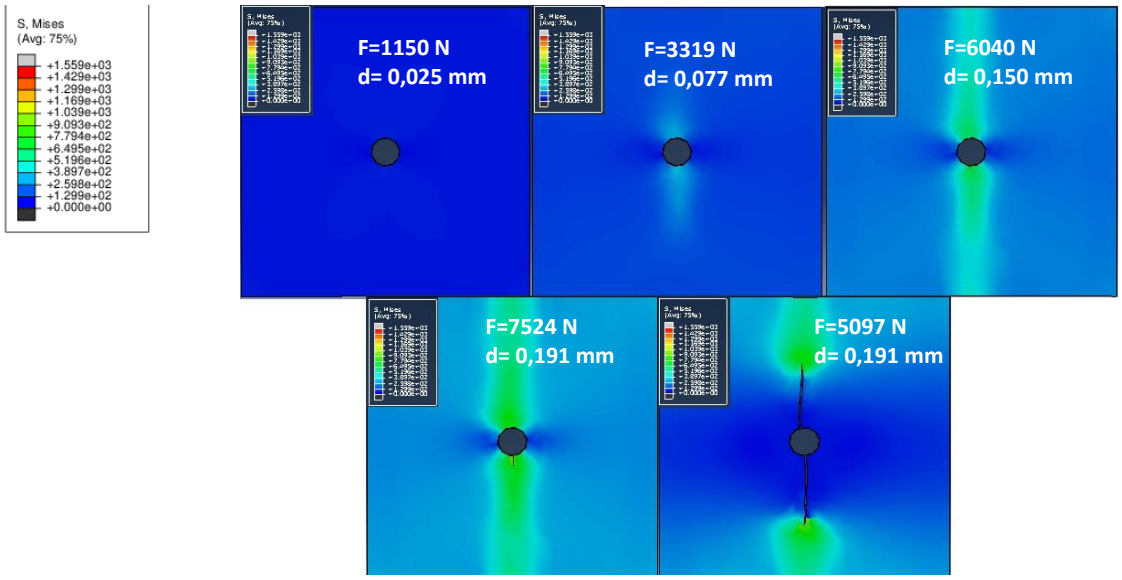

Figure 46. XFEM stresses evolution in "Reference case"

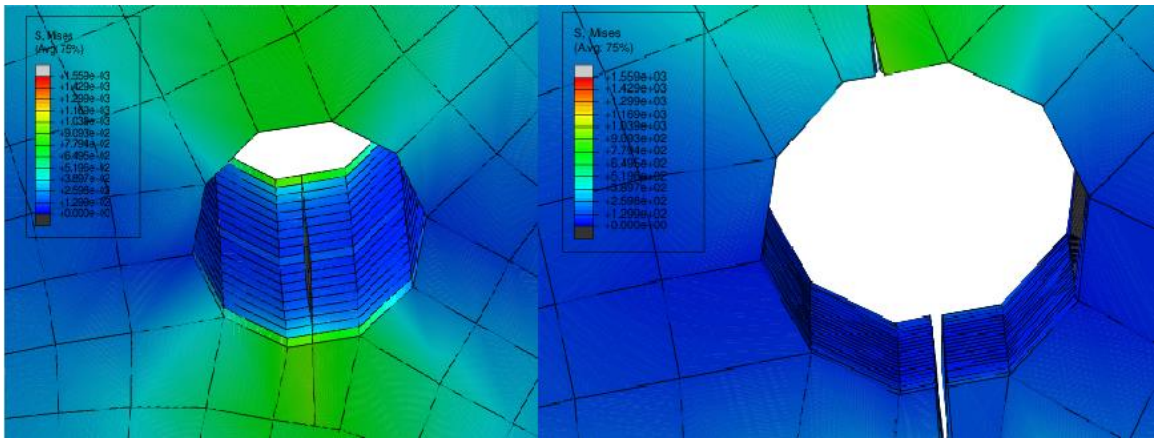

Figure 47. Crack before and after the material failure

So that the results will be collected in the following graphs (Figure 48, Figure 49, Figure 50, Figure 51) gathering in each force-displacement curve the results belonging to each stacking sequence for the three radius of the hole. Likewise, Table 12, Table 13, Table 14 and Table 16 collect the different values of maximum load, displacements at plate failure and stiffness and strength for the different stacking sequences.

Regarding the plate strength, it can be observed through the Table 13 and Table 16 that “Case I” and “Case III” present the maximum loads (out of four different cases). These two configurations present the maximum number of 0º plies of all the four studied cases, which provides to the laminate a greater resistance in this direction. The same happens for the stiffness, because 0º direction is the direction of application of the imposed stretching displacements (tensile loading). Likewise, as the radius of the hole increases, it can be appreciated a stiffness reduction. The plates with smaller holes are stiffer, so they experience higher stresses for the same applied strain, which mean that they damage earlier. This last statement is verified after checking the following figures and tables: when the radius increases, the displacement at failure is higher and the ultimate load is lower due to the lower net cross-section of the plate. Next, each case is analyzed separately.

Reference case

In this case, $[0,90_8,0,90_8,0]$, it can be observed in Figure 48 that the curve does not follow a completely linear behavior until failure. Around loads close to 2500-3200 N, it can be seen a small drop in the curves that corresponds to the first failure due to the breaking of all the 90º plies and the central 0º ply. After that, the load continues growing until the final failure, which is achieved when the maximum load is reached – see Table 12. Therefore, this case corresponds to a weak laminate under tensile loads due to the large numbers of 90º plies, which are not able to distribute correctly the efforts in the composite.

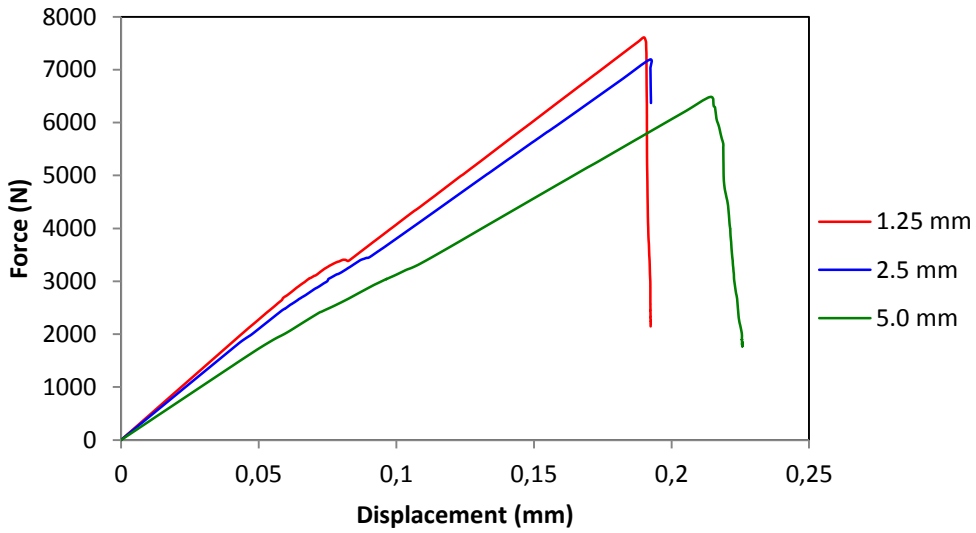

Figure 48. Force-displacement curves obtained from XFEM analyses of the "Reference case" for the different hole radii

Table 12. Mechanical properties obtained from XFEM analyses of the “Reference case”

Hole size [mm]	Maximum Load [N]	Displacement at failure [mm]	Stiffness [N/mm]	Ultimate Strength [MPa]
1.25	7524	0,191	4,60E+04	110,0
2.5	7191	0,192	4,28E+04	105,1
5.0	6485	0,214	3,40E+04	94,8

Case I

This laminate, $[90,0_8,90,0_8,90]$, is dominated by the 0º plies therefore it will present a greater resistance until tensile loading. The first ply where the failure appears is the central 90º ply, but in this case, failure will take place later and it will be more progressive because the 0º plies will be able to distribute the stresses better. After the failure of 90º layers (at loads between 11289-12020-14973 N for the different hole radii 1.25-2.5-5.0 mm), the damage spreads almost instantaneously to the rest of the plies. For which reason, the obtained curves shown in Figure 49 are almost linear up to the final failure.

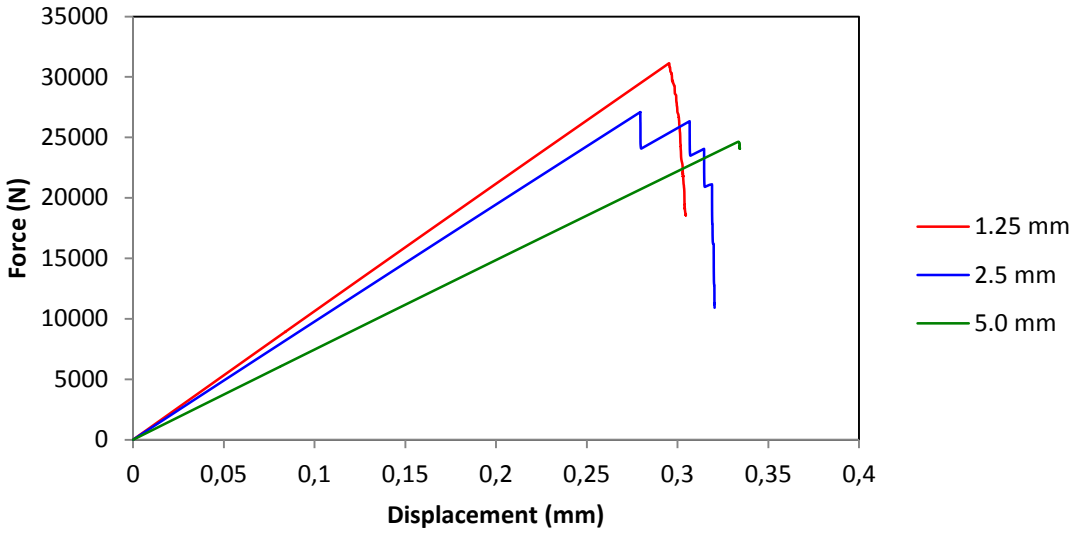

Figure 49. Force-displacement curves obtained from XFEM analyses of the "Case I" for the different hole radii

Table 13. Mechanical properties obtained from XFEM analyses of the "Case I"

Hole size [mm]	Maximum Load [N]	Displacement at failure [mm]	Stiffness [N/mm]	Ultimate Strength [MPa]
1.25	31131	0,295	1,07E+05	455,1
2.5	27092	0,320	9,80E+04	396,1
5.0	24600	0,334	7,54E+04	359,6

Case II

For this case, [90_8,0,0,0,90_8], and in the same way as in the “Reference case”, it can be observed in Figure 50 some irregularities at 40% of the maximum load (between 2608-2920-3177 N for the different hole radii 5.0-2.5-1.25 mm), corresponding to the onset of the failure. This is because the 90º plies break completely before the onset of the 0º plies breakage. Whose failure occurs at the maximum load, corresponding to the plate fracture. As it happened in the “Reference case”, the large number of 90º plies, makes this laminate weaker than those of the Cases I and III. The 0º plies concentrate all the stresses caused by the imposed stretching displacements and due to the low number of these layers, the failure will take place quickly. In spite of the fact that “Reference case” and “Case II” present the same number of 0º and 90º plies, it can be appreciated through Table 12 and Table 14 that “Case II” presents better values of strength than the “Reference case”. This last is due to the different distribution of the 0º plies into the laminate. The three 0º plies stacked together in the midline zone of the laminate (Case II) seems to favor the strength of the laminate. Conversely, the same three plies stacked separately lead to lower strength of the laminated plate because they are connected through 90º layers that weaken the resistance of the group. Table 15 shows the ratios between some variables (maximum load - F_{max}, displacement at failure - d_f, elastic stiffness - K) of Reference Case and Case II. It is obvious that the stiffness is very similar but the strength profit is better using [90_8, 0, 0, 0, 90_8] rather than [0, 90_8, 0, 90_8, 0].

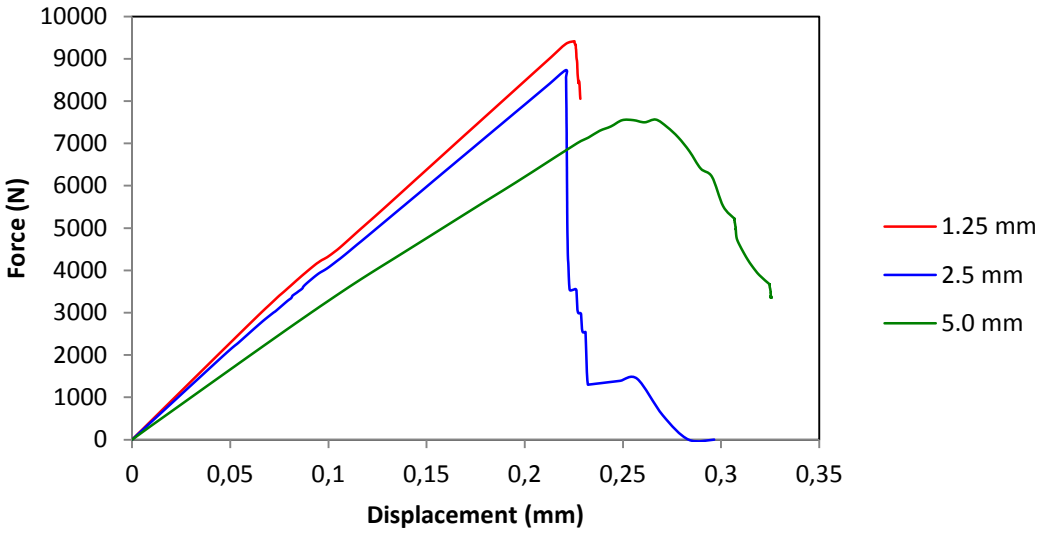

Figure 50. Force-displacement curves obtained from XFEM analyses of the "Case II" for the different hole radii

Table 14. Mechanical properties obtained from XFEM analyses of the "Case II"

Hole size [mm]	Maximum Load [N]	Displacement at failure [mm]	Stiffness [N/mm]	Ultimate Strength [MPa]
1.25	9414	0,225	4,60E+04	137,6
2.5	8561	0,221	4,30E+04	125,2
5.0	7562	0,266	3,34E+04	110,6

Table 15. Comparison between Reference Case and Case II (XFEM analyses)

Hole size [mm]	$F_{max.R}/F_{max.II}$	$d_{f.R}/d_{f.II}$	K_R/K_I
1.25	0.800	0.849	1
2.5	0.840	0.869	0.995
5.0	0.858	0.805	1.018

Case III

This last case, $[0_8,90,90,90,0_8]$, follows a similar behavior to the "Case I" due to the domain of the 0º plies. The onset of the failure in this "Case III" occurs at lowers loads (8138-8867-9541 N, for 5.0-2.5-1.25 mm) than in the "Case I". However, the final failure of the laminate takes place almost at the same time in both cases, as it can be seen in Table 13 and Table 16. In the same way as in the "Case I", the failure of the 90º plies takes place earlier, spreading progressively almost until the final failure. This is due to the good distribution of the stresses made by the high number of 0º plies. So an almost linear curve is plotted in Figure 51 until final failure of the analyzed plate.

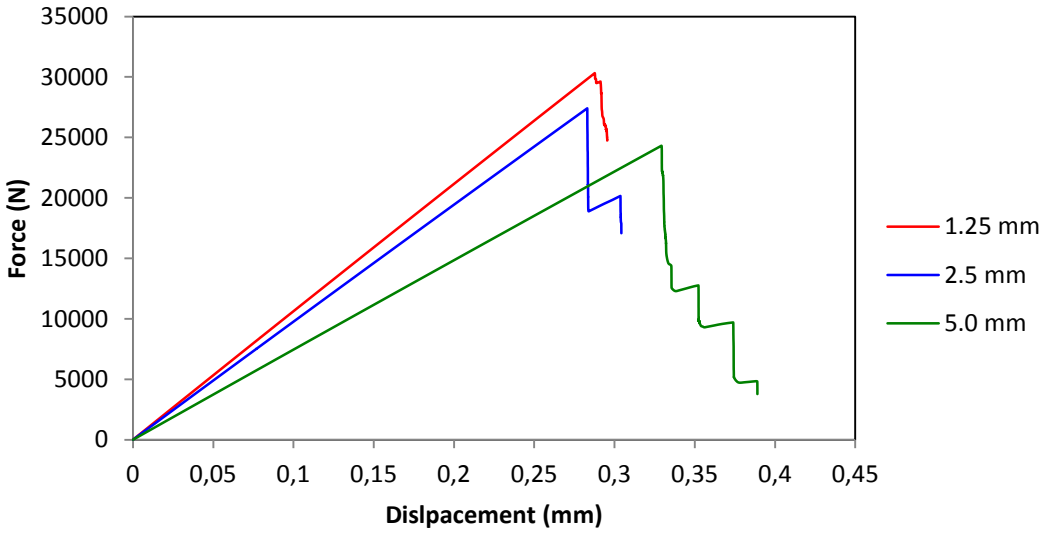

Figure 51. Force-displacement curves obtained from XFEM analyses of the "Case III" for the different hole radii

Table 16. Mechanical properties obtained from XFEM analyses of the "Case III"

Hole size [mm]	Maximum Load [N]	Displacement at failure [mm]	Stiffness [N/mm]	Ultimate Strength [MPa]
1.25	30314	0,288	1,07E+05	443,2
2.5	27407	0,304	9,80E+04	400,7
5.0	24312	0,329	7,50E+04	355,4

Table 17 shows the ratios between some variables (maximum load - F_{max}, displacement at failure - d_f, elastic stiffness - K) of Case I and Case III. The obtained ratios are very similar for both Cases I and

III. The large number of 0º plies being placed together cause that the position of the only three 90º plies has not a decisive impact in the results.

Table 17. Comparison between Case I and Case III (XFEM analyses)

Hole size [mm]	$F_{max.I}/F_{max.III}$	$d_{f.I}/d_{f.III}$	K_I/K_{III}
1.25	1.027	1.024	1
2.5	0.989	1.053	1
5.0	1.012	1.015	1.005

Influence of the radius of the hole

Thanks to Table 18, it is possible to observe how the increase of the radius of the hole affects to the stiffness, maximum load and displacement at failure. The plates with bigger holes present low values of maximum loads and stiffness while they experience higher displacements at failure.

Table 18. Influence of the radius of the hole in strength and stiffness of laminate plates (XFEM analyses)

		Reference case	Case I	Case II	Case III
Maximum load	$F_{max,2.5}/F_{max,1.25}$	0.956	0.870	0.909	0.904
	$F_{max,5.0}/F_{max,1.25}$	0.862	0.790	0.803	0.802
Displacement at failure	$d_{f,2.5}/d_{f,1.25}$	1.005	1.085	0.982	1.056
	$d_{f,5.0}/d_{f,1.25}$	1.120	1.132	1.182	1.142
Stiffness	$K_{2.5}/K_{1.25}$	0.930	0.916	0.935	0.916
	$K_{5.0}/K_{1.25}$	0.739	0.705	0.726	0.701

5.3.2 Hashin-based results and discussion

In this section, the analysis of the damage suffered by the material is now studied using the Hashin criterion for composites, which predict the first ply failure and damage propagation but no crack formation is allowed (unlike the crack prediction and spread considered by XFEM). As it was said previously, Hashin criterion detects the damage once any of the following failure modes are achieved: (i) fiber tensile failure, (ii) matrix tensile failure, (iii) fiber compressive failure and (iv) matrix compressive failure. In order to detect the damage evolution, the values of the critical energy release rate of the four damage modes are necessary G_{cft} (critical energy release rate for fiber tensile failure), G_{cmt} (critical energy release rate for matrix tensile failure), G_{cfc} (critical energy release rate for fiber compressive failure), G_{cmc} (critical energy release rate for matrix compressive failure), which contrasts with XFEM models where both onset and evolution of damage are predicted in terms of critical ERR only. This is due to fact that the damage addressed by Hashin's method is intralaminar while XFEM analyzes the interlaminar damage through the whole laminate. However, in this work, a first approach

was done using the same value of ERR in XFEM for all the four damage modes – this assumption was adopted in order to obtain an equivalent approach between Hashin's method and XFEM [40, 41] and investigate the differences between the ensuing results.

In case of Hashin-based analyses, the evolution of the damage is shown in Figure 52 and Figure 53 for the 0º and 90º plies in "Reference case" for different loading levels. In Figure 52 is possible to appreciate how the damage extends in a perpendicular direction to the applied load for the 0º plies. Figure 53 shows how the damage grows through the entire plate in the 90º plies, due to their low strength regarding the transversal loads.

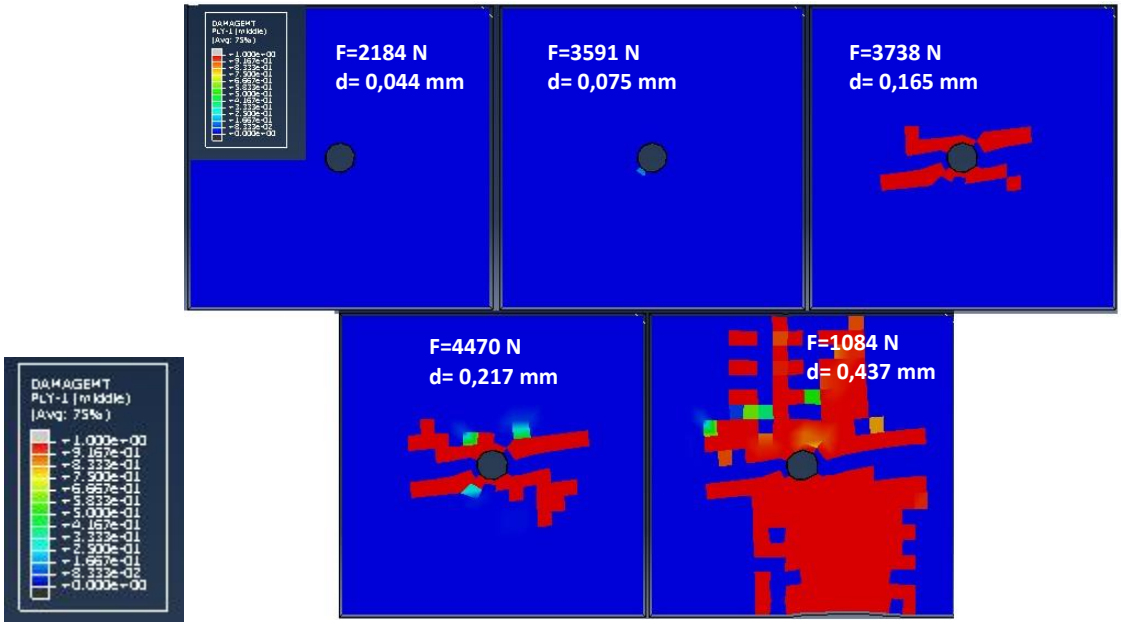

Figure 52. Hashin damage evolution for 0º plies in "Reference case"

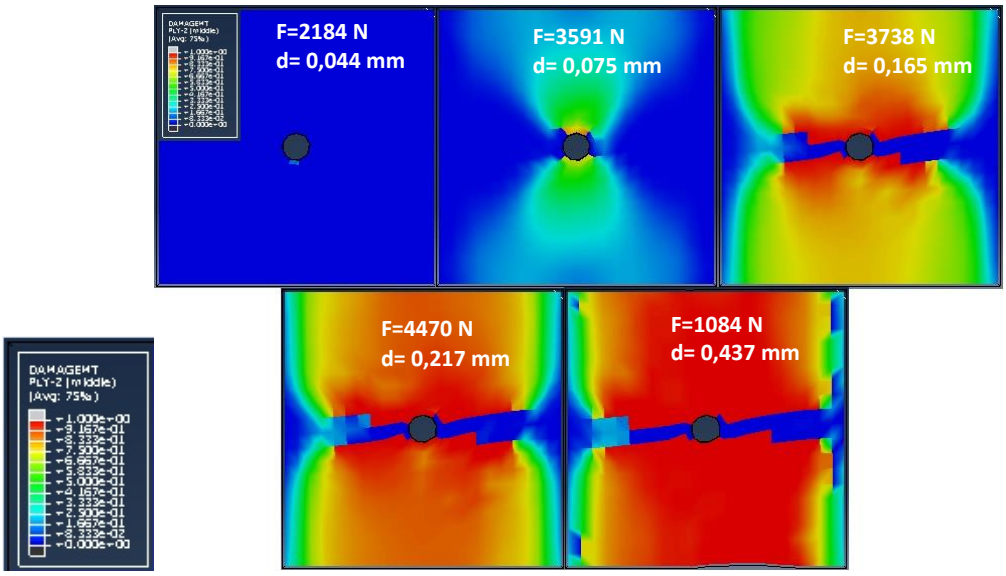

Figure 53. Hashin damage evolution for 90º plies in "Reference case"

Likewise, it is important to show the evolution of different stresses between the 0º and 90º plies that are presented in the laminated plate. The stresses experienced by the 0º plies are higher than those of the 90º plies, which is reasonable after applying a tensile load in 0º direction. The evolution of the stresses for the 0º plies tends to increase in the perpendicular direction to this tensile load, which is consistent with the mode I of fracture that is expected to occur (Figure 54). However, for the 90º plies the stresses tend to grow in the applied load direction due to the fact that these plies are designed to support transverse loads (Figure 55).

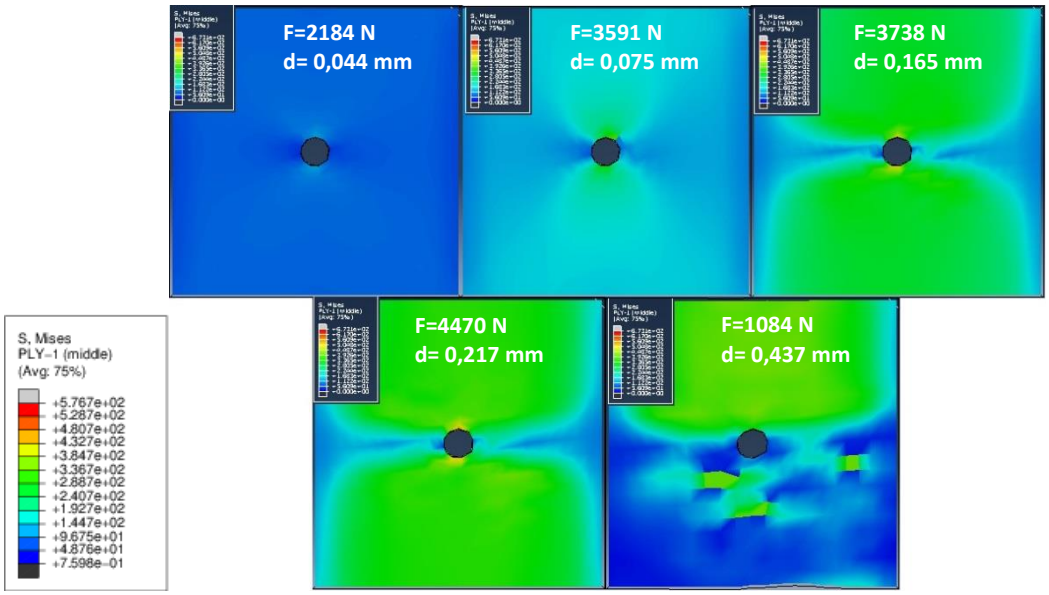

Figure 54. Hashin stresses evolution for 0º plies in “Reference case”

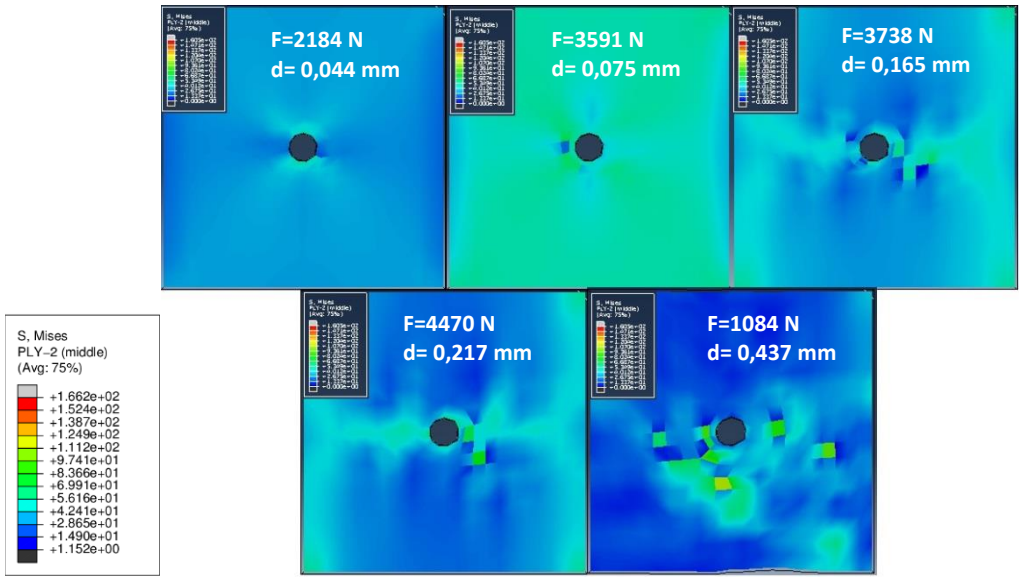

Figure 55. Hashin stresses evolution for 90º plies in "Reference case"

After showing the damage and stresses evolution, the following figures (Figure 56, Figure 57, Figure 58 and Figure 59) gather the force-displacement curves belonging to each stacking sequence for the three hole radii. Likewise, Table 19, Table 20, Table 21, and Table 23 collect the different values of maximum load, displacements at failure, stiffness and strength for the different stacking sequences which have been analyzed.

Therefore, based on the obtained results it can be observed that curves of Figures 57 and 59 ("Case I" and "Case III", respectively) present an almost linear behavior until the maximum load is reached, while those of Figures 56 and 58 ("Reference Case" and "Case II", respectively) experience a more irregular behavior after the first failure. Additionally, the degradation of stiffness after failure is much more severe in Hashin-based analyses than the crack growth in XFEM analyses. So, as it has been previously exhibited for the XFEM analyses, the onset of the first ply failure for the "Case I" and "Case III" started at loads near 9000-13000 N, spreading progressively until loads close to the final failure.

Regarding "Reference Case" and "Case II", most of the layers are 90º oriented, so they will have a low resistance when a tensile load is applied. Therefore, those 90º layers will be the first to fail, followed by the 0º oriented layers. Those layers will support most of the load as they are oriented in the load direction. However, for Case I and Case III, there will be a better overall strength as most of the layers are 0º oriented. For these two cases, failure of 90º layers will take place later, and it will be more progressive. At the end, 0º layers will fail due to overload.

Likewise, and for all the possible stacking sequences, it can be observed a reduction in the stiffness when increasing the radius hole as it happened in the XFEM analyses. In terms of the displacements, it is possible to appreciate how, before the first failure, they are bigger when the radius of the hole increases.

On the other hand, and confirming the XFEM results previously obtained, the more resistant laminates are those which belong to the "Case I" and "Case III" since they are the ones that have more plies faced in the direction of application of the imposed displacements (0º direction).

Reference case

For this stacking sequence, $[0,90_8,0,90_8,0]$, Figure 56 shows that the onset of the failure in the first damaged ply starts at loads around 2480-3296-3500 N for the different hole radii (5.0-2.5-1.25 mm). This first failure occurs for the 90º plies, which are the weak layers in this laminate under tensile loading. After the onset of the failure of these 90º layers, they will continue deteriorating until the full failure of the ply. Interesting is the case corresponding to the 2.5 mm radius hole (curve plotted in blue) where the first drop (3641 N, 0,181 mm) does not mean the ultimate failure. The fiber breakage does not happen instantaneously at this point, occurring the ultimate failure when the second drop (2529N, 0,233 mm) is reached.

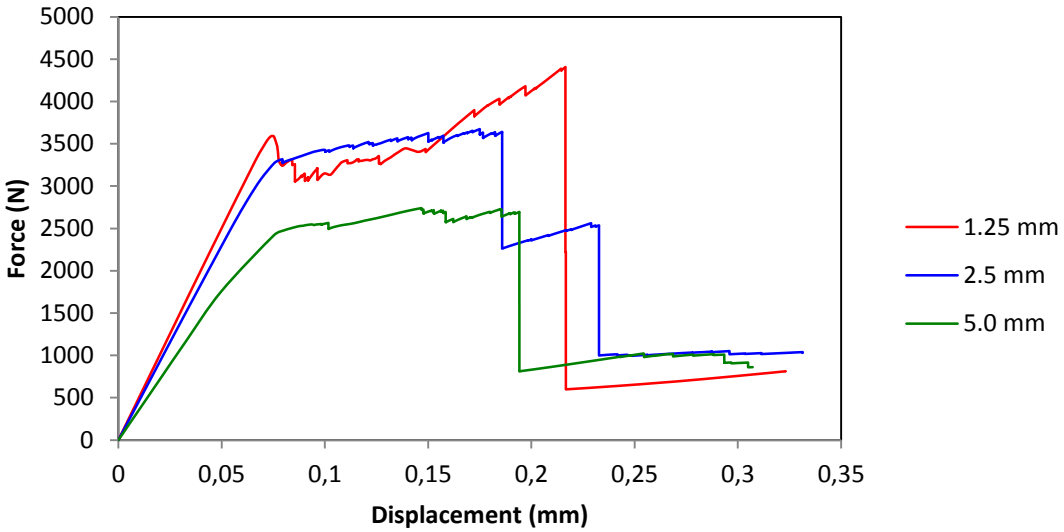

Figure 56. Force-displacement curves obtained from Hashin-based analyses of the "Reference case" for the different hole radii

Table 19. Mechanical properties obtained from Hashin-based analyses of the "Reference case"

Hole size [mm]	Maximum Load [N]	Displacement at failure [mm]	Stiffness [N/mm]	Strength [MPa]
1.25	4407	0,216	5,03E+04	64,4
2.5	3641	0,233	4,62E+04	53,2
5.0	2730	0,194	3,57E+04	39,4

Case I

In this case, [90,0_8,90,0_8,90], the onset of the failure of the first damaged ply starts at loads between 12900-14800-15000 N, for the different hole radii (5.0-2.5-1.25 mm), and will spread progressively until loads close to 28000 N. As it happened with the XFEM results of “Case I”, the first damaged plies will be the 90º plies.

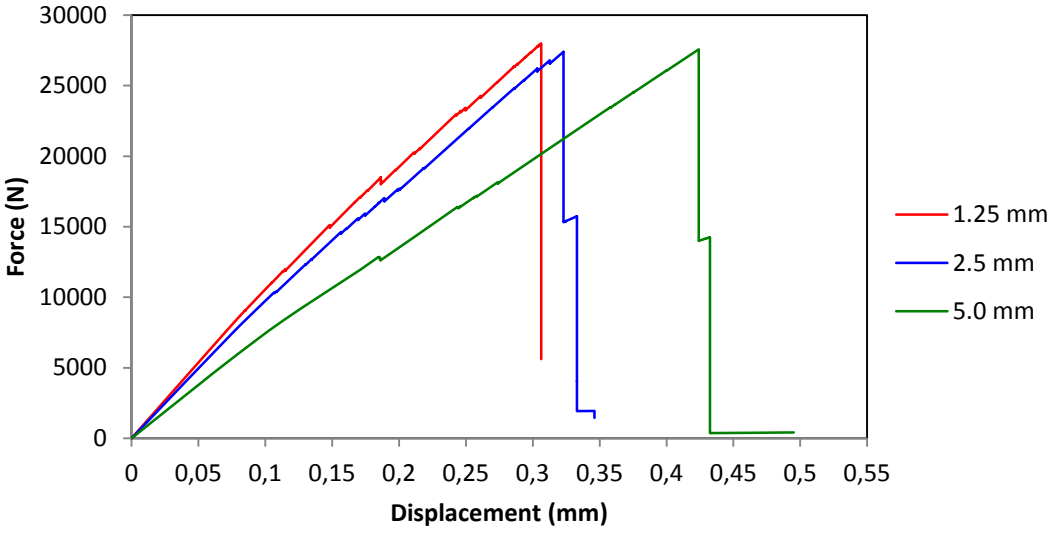

Figure 57. Force-displacement curves obtained from Hashin-based analyses of the "Case I" for the different hole radii

Table 20. Mechanical properties obtained from Hashin-based analyses of the "Case I"

Size hole [mm]	Maximum Load [N]	Displacement at failure [mm]	Stiffness [N/mm]	Strength [MPa]
1.25	27994	0,306	1,07E+05	409,3
2.5	27392	0,323	9,95E+04	400,5
5.0	27569	0,424	7,58E+04	403,1

Case II

For this stacking sequence, $[90_8,0,0,0,90_8]$, Figure 56 shows that the onset of the failure in the first damaged ply starts at loads around 2270-3030-3500 N for the different hole radii (5.0-2.5-1.25 mm). As it happened for the “Reference case”, this first failure occurs for the 90º layers, which are the weak plies in this laminate under tensile loading. After the onset of the failure of these 90º layers, the plies will continue deteriorating until the full failure at loads between 4500-5290-6180 N for the different hole radii (5.0-2.5-1.25 mm). In the same way that happened in the “Reference case”, the case corresponding to the 2.5 mm radius hole (curve plotted in blue) shows two significant drops before the ultimate failure.

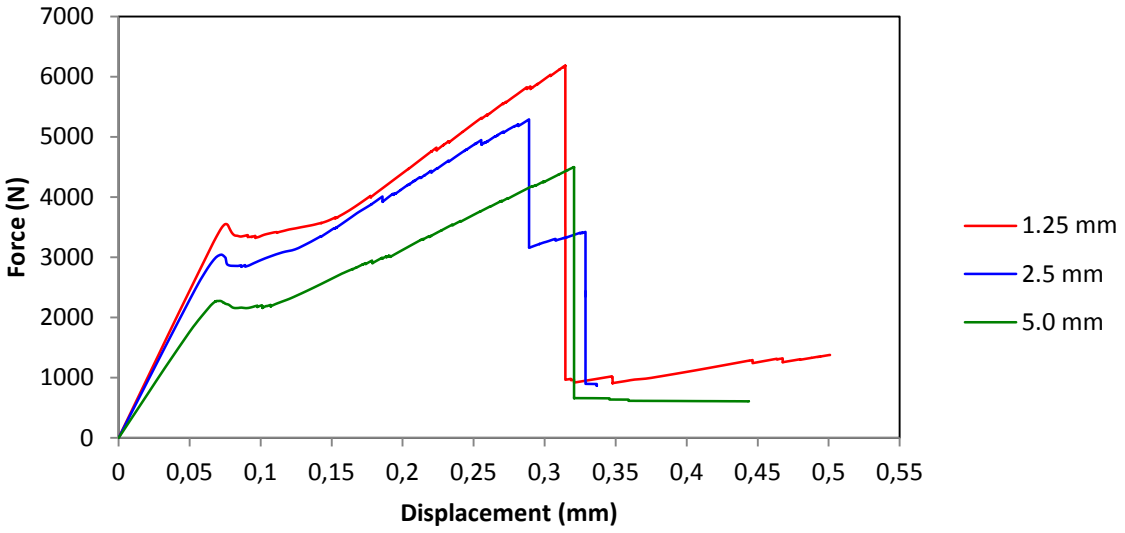

Figure 58. Force-displacement curves obtained from Hashin-based analyses of the "Case II" for the different hole radii

Table 21. Mechanical properties obtained from Hashin-based analyses of the "Case II"

Hole size [mm]	Maximum Load [N]	Displacement at first failure [mm]	Stiffness [N/mm]	Strength [MPa]
1.25	6181	0,311	4,90E+04	90,4
2.5	5289	0,325	4,62E+04	77,3
5.0	4497	0,321	3,57E+04	65,8

Table 22 shows the ratios between some variables (maximum load - F_{max}, displacement at failure - d_f, elastic stiffness - K) of Reference Case and Case II. It is obvious that the stiffness is very similar but

the strength profit is better using [90_8, 0, 0, 0, 90_8] rather than [0, 90_8, 0, 90_8, 0]. As it happened in the XFEM analyses, the three plies stacked together in the midline zone of the laminate ("Case II") seems to favor the strength of the laminate.

Table 22. Comparison between Reference Case and Case II (Hashin-based analyses)

Hole size [mm]	$F_{max.R}/F_{max.II}$	$d_{f.R}/d_{f.II}$	K_R/K_{II}
1.25	0.713	0.695	1.027
2.5	0.688	0.717	1
5.0	0.599	0.604	1

Case III

In this case, [0_8,90,90,90,0_8], the onset of the failure of the first damaged ply starts at loads between 8300-10520-11843 N, for the different hole radii (5.0-2.5-1.25 mm), and will spread progressively until loads close to 27500-31370-27200 N, for the different hole radii (5.0-2.5-1.25 mm). As it happened with the "Case III"'s analyses with XFEM, the first damaged plies will be the 90º plies.

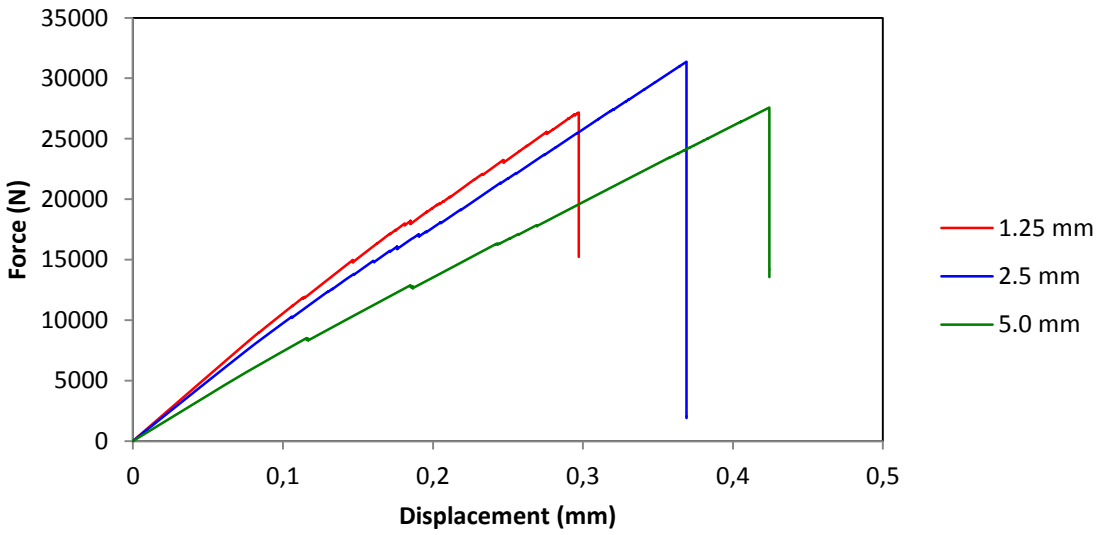

Figure 59. Force-displacement curves obtained from Hashin-based analyses of the "Case III" for the different hole radii

Table 23. Mechanical properties obtained from Hashin-based analyses of the "Case III"

Hole size [mm]	Maximum Load [N]	Displacement at failure [mm]	Stiffness [N/mm]	Strength [MPa]
1.25	27168	0,297	1,08E+05	397,2
2.5	31369	0,369	9,95E+04	458,6
5.0	27582	0,424	7,58E+04	403,2

Table 24 shows the ratios between some variables (maximum load - F_{max}, displacement at failure - d_f, elastic stiffness - K) of Case I and Case III. The obtained ratios are very similar for both Cases I and III. The large number of 0º plies being placed together cause that the position of the only three 90º plies has not a decisive impact in the results.

Table 24. Comparison between Case I and Case III (Hashin-based analyses)

Hole size [mm]	$F_{max.I}/F_{max.III}$	$d_{f.I}/d_{f.III}$	K_I/K_{III}
1.25	1.030	1.030	0.991
2.5	0.873	0.875	1
5.0	0.999	1	1

Influence of the hole diameter

After carrying out the different Hashin-based analyses, Table 25 gathers a comparison between the different hole radii in terms of *maximum load*, *displacement at failure* and *stiffness*. For all the different stacking sequences, there is a reduction of the stiffness as the hole radius increases. For the "Case I" and "Case II", the displacement at failure increases when the radius is bigger, while "Reference case" and "Case II" present the inverse behavior. Regarding the maximum loads, they are lower when the radius is increased in "Reference case" and "Case II", while "Case I" and "Case III" follow different behaviors.

Table 25. Influence of the radius hole in strength and stiffness of laminate plates (Hashin-based analyses)

		Reference case	Case I	Case II	Case III
Maximum load	$F_{max,2.5}/F_{max,1.25}$	0.826	0.978	0.856	1.155
	$F_{max,5.0}/F_{max,1.25}$	0.612	0.985	0.728	1.015
Displacement at failure	$d_{f,2.5}/d_{f,1.25}$	1.079	1.056	1.045	1.242
	$d_{f,5.0}/d_{f,1.25}$	0.898	1.386	1.032	1.428
Stiffness	$K_{2.5}/K_{1.25}$	0.918	0.930	0.943	0.921
	$K_{5.0}/K_{1.25}$	0.710	0.708	0.729	0.702

5.3.3 Comparison between XFEM and Hashin-based results

In this section, a comparison between the XFEM and Hashin-based results will be carried out in order to show the differences that occur when using one of these methods. With this purpose, the curves obtained with both methods for each stacking sequence are overlapped in Figures 60 to 63, while a comparison between the main results of the two methods is gathered in the Tables 26 to 29. Also it is necessary to bear in mind that the analyses performed by Hashin's criterion are based on the assumption of using a similar value of fracture energy for the four failure modes. Regarding the computational efficiency of both methods, the analyses carried out with XFEM took twice the amount of time than the analyses done with Hashin-based method (36000 seconds in average for XFEM and

18000 seconds in average for Hashin-based method). Bearing in mind that the analyses were done using the following processor: “Intel® Core™ i3-2330 M CPU @ 2.20 GHz.

Reference case

For this case, the Figure 60 shows how the values obtained with Hashin are in good agreement with XFEM until the onset of the failure of the first ply. After this point, and as it was specified in the previous section, the force-displacement curves of both methods differ greatly. The differences in the F-d curves for both methods after first failure occur because this “Reference case” is dominated by the 90º plies and the transversal damage criterion in Hashin was defined in an approximate way (remember that the same value of ERR was used for all the four Hashin damage modes).

As Table 26 shows, the displacements and loads at first failure are very similar for both XFEM and Hashin-based cases. Higher loads at “first failure” are reached with the Hashin –based method while the stiffness values are also in good agreement between the two methods. Very different values of maximum loads are obtained for both methods and a significant reduction in the slopes of the F-d curves could be observed after the first failure for the Hashin-based analyses.

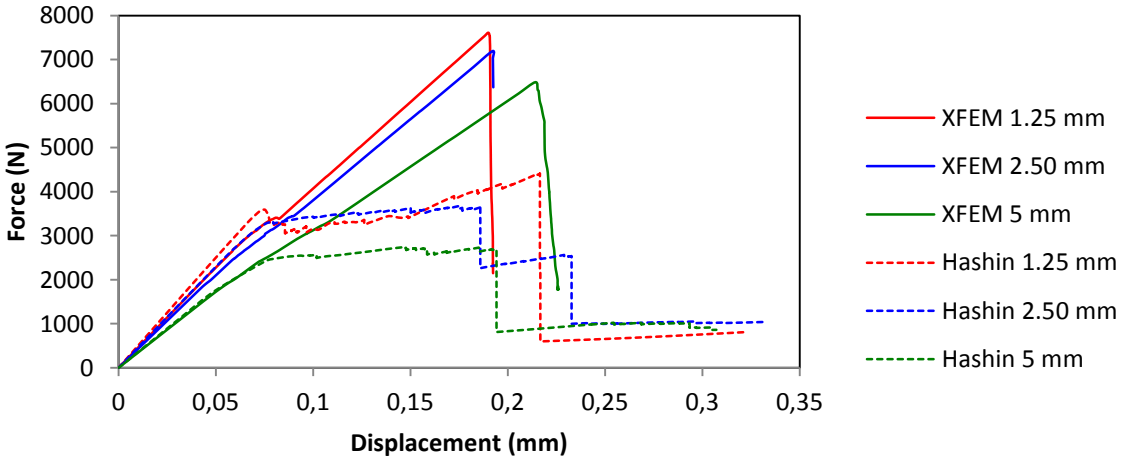

Figure 60. Comparison between XFEM and Hashin-based method for the “Reference case”

Table 26. Comparison between XFEM and Hashin-based results for the “Reference case”

	Hole size [mm]					
	1.25		2.5		5.0	
	XFEM	Hashin	XFEM	Hashin	XFEM	Hashin
First failure load [N]	2973	3539	2955	3296	2469	2486
Displacement at first failure [mm]	0,074	0,072	0,074	0,081	0,075	0,082
Maximum load [N]	7524	4407	7191	3641	6485	2695
Displacement at failure [mm]	0,191	0,216	0,192	0,233	0,214	0,194
Stiffness [N/mm]	4,60E+04	5,03E+04	4,28E+04	4,62E+04	3,40E+04	3,57E+04

Case I

In this case, similar values of force and displacements are obtained with both Hashin and XFEM methods until the ultimate failure, as shown in Figure 61. In this case, the first ply failure follows a more progressive and linear behavior due to the large number of 0º plies which distribute better the stresses between the laminate. As it is shown in Table 27, Hashin-based analyses give higher values of loads and displacements at "first failure" than the values obtained with XFEM, while the stiffness values are very similar for both two methods. Regarding the maximum load, the values of Hashin-based analyses differ approximately ±3000 N from the XFEM values.

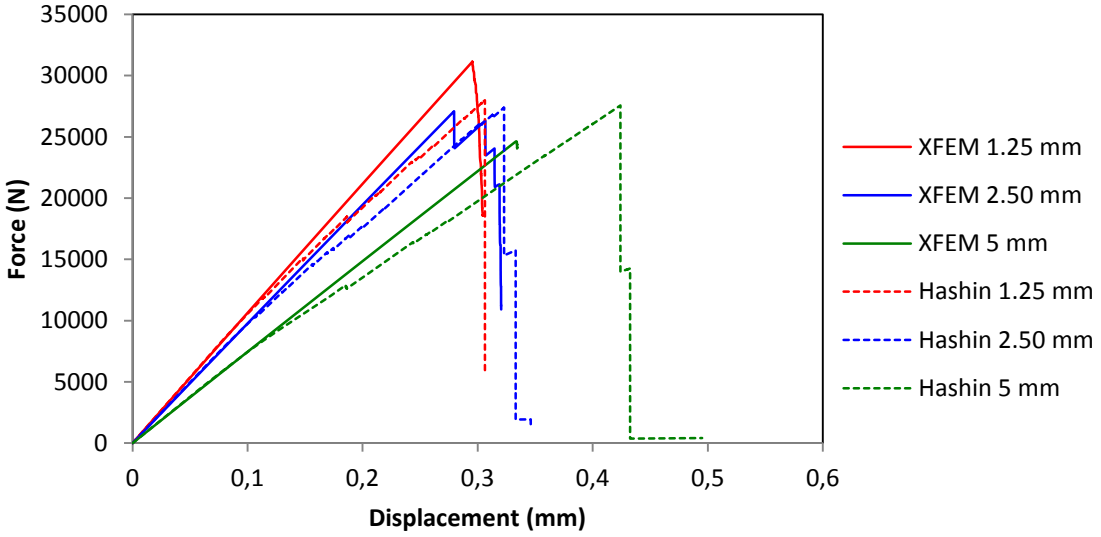

Figure 61. Comparison between XFEM and Hashin-based method for the "Case I"

Table 27. Comparison between XFEM and Hashin-based results for the "Case I"

	Hole size [mm]					
	1.25		2.5		5.0	
	XFEM	Hashin	XFEM	Hashin	XFEM	Hashin
First failure load [N]	13333	14973	12020	14843	11289	12898
Displacement at first failure [mm]	0,125	0,147	0,125	0,161	0,152	0,19
Maximum load [N]	31131	27994	27092	27392	24600	27569
Displacement at failure [mm]	0,295	0,306	0,320	0,323	0,334	0,424
Stiffness [N/mm]	1,07E+05	1,07E+05	9,80E+04	9,95E+04	7,54E+04	7,58E+04

Case II

For this case, and as it happened in the "Reference case", the Figure 62 shows a similar behavior until the appearance of the "first failure", differing the curves since this point. The differences in the F-d curves for both methods after first failure occur because this "Case II" is dominated by the 90º plies

and the transversal damage criterion in Hashin was defined in an approximate way (remember that the same value of ERR was used for all the four Hashin damage modes).

For both methods, Table 28 shows how the load and displacements values obtained at "first failure" are almost the same, differing in a small amount. In the same way than in the "Reference case", a very pronounced reduction in the slope of the F-d curves could be observed after the first failure for the Hashin-based analyses.

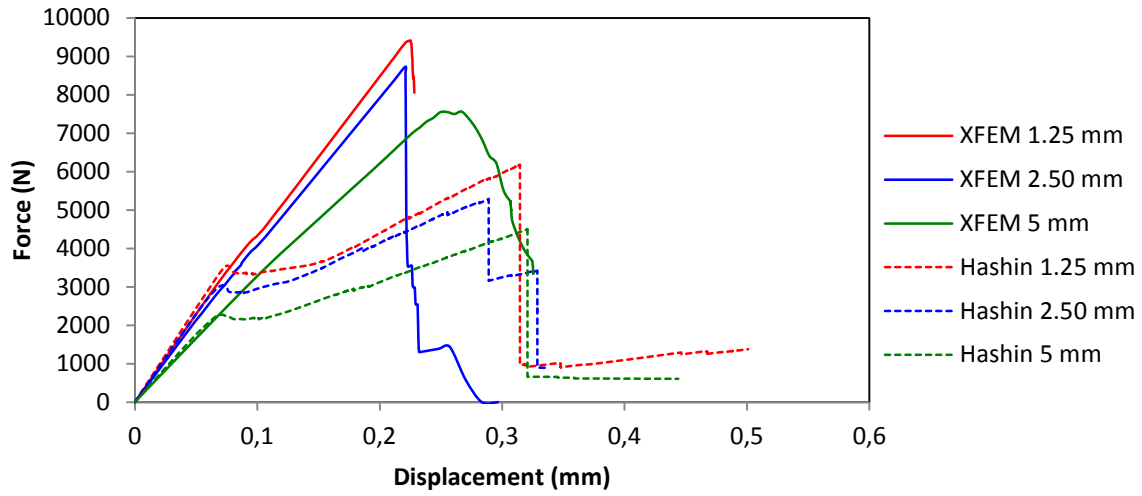

Figure 62. Comparison between XFEM and Hashin-based method for the "Case II"

Table 28. Comparison between XFEM and Hashin-based results for the "Case II"

	Hole size [mm]					
	1.25		2.5		5.0	
	XFEM	Hashin	XFEM	Hashin	XFEM	Hashin
First failure load [N]	3177	3510	2920	3033	2608	2273
Displacement at first failure [mm]	0,076	0,073	0,07	0,071	0,079	0,07
Maximum load [N]	9414	6181	8561	5289	7562	4497
Displacement at failure [mm]	0,225	0,311	0,221	0,325	0,266	0,321
Stiffness [N/mm]	4,60E+04	4,90E+04	4,30E+04	4,62E+04	3,34E+04	3,57E+04

Case III

The Figure 63 represent a superimposing of the different curves belonging to the analyses did with XFEM and Hashin, showing a similar behavior to the "Case I" previous mentioned. Hashin-based analyses give higher values of loads and displacements at "first failure" than the values obtained with XFEM, while the stiffness values are very similar for both two methods. Regarding the maximum load, the values of Hashin-based analyses differ approximately ±3000 N from the XFEM values-see Table 29.

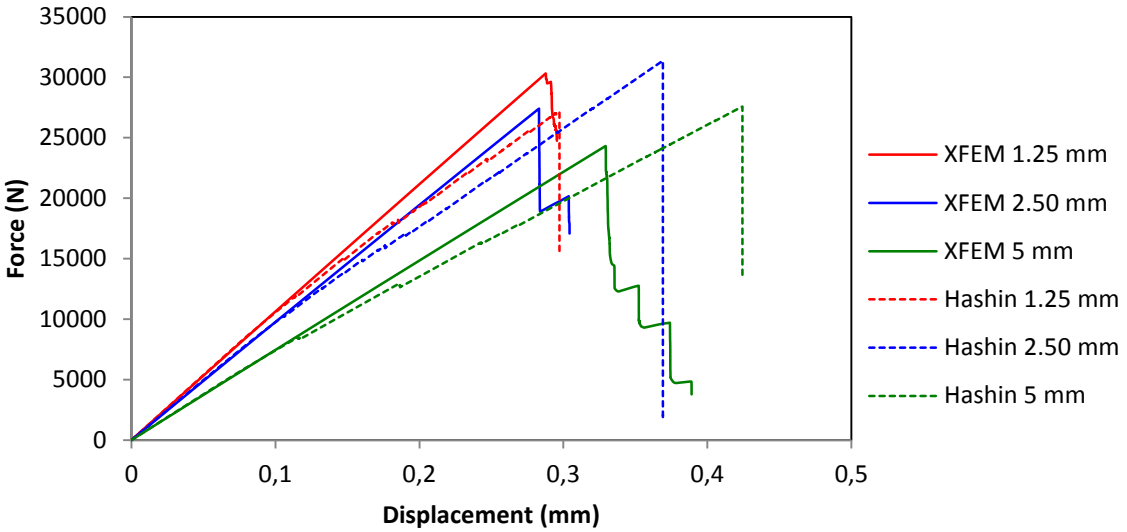

Figure 63. Comparison between XFEM and Hashin-based method for the "Case III"

Table 29. Comparison between XFEM and Hashin-based results for the “Case III”

	Hole size [mm]					
	1.25		2.5		5.0	
	XFEM	Hashin	XFEM	Hashin	XFEM	Hashin
First failure load [N]	9541	11843	8867	10519	8138	8320
Displacement at first failure [mm]	0,097	0,124	0,091	0,11	0,11	0,121
Maximum load [N]	30314	27168	27407	31369	24312	27582
Displacement at failure [mm]	0,288	0,297	0,304	0,369	0,329	0,424
Stiffness [N/mm]	1,07E+05	1,08E+05	9,80E+04	9,95E+04	7,50E+04	7,58E+04

Chapter 6

CONCLUSIONS AND FUTURE DEVELOPMENTS

This dissertation consisted of six chapters, briefly resumed as follows:

- Chapter 1 included a little review about the different materials used in the aviation industry throughout the history. Some cases of damage in aircraft were presented in order to show the importance of the study of the onset of the damage in aircraft structures. Finally the motivations and the targets of this project were exhibited at the end of the chapter.
- In Chapter 2 a review of composites materials was presented. The main concepts about these materials were presented as well as the different applications in aviation.
- Chapter 3 described the different methods available to predict damage in composite materials. Some of them only will predict the first ply failure as “Failure Criteria” while others will predict the damage evolution through the entire laminate as “Continuum Damage Mechanics” and “Discrete Damage Model”.
- In Chapter 4 three previous studies on composite damage were presented.
- Some parametric studies were carried out in Chapter 5 in order to compare the different results obtained after using the both XFEM and Hashin-based methods. Plates with different hole sizes and stacking sequences were analyzed during these parametric studies.
- Finally, this chapter (Chapter 6) presents the main conclusions and future recommendations.

6.1 Main Achievements and Conclusions

The aim of this project was the study of the damage and fracture propagation in fiber reinforced composites and its response to a mechanical action. To achieve these purposes, the finite element software Abaqus was used in order to find out the accuracy of different failure criteria when analysing fibre composite laminates made of glass/vinylester. The damage and failure of plates with different radius of the hole and several layer configurations was analyzed through two different methods: (i) eXtended Finite Element Method (XFEM) and (ii) Hashin-based method.

In total, 24 different analyses are done, through XFEM and Hashin-based method, corresponding to plates with three different hole radii (1.25 mm radius; 2.5 mm radius; and 5.0 mm radius) and four different stacking sequences (“Reference case”, “Case I”, “Case II” and “Case III”). In order to validate the numerical model developed in the current work, a stiffness validation of the XFEM and Hashin-based analyses was made. The results obtained with both methods were compared with the experimental test results presented by Moure et al. [22]. Obtaining good agreement in the behavior of the three cases, with small differences due to the different finite elements used (solid elements in case of XFEM and shell in case of Hashin-based analysis).

Thanks to XFEM, it was possible to detect the onset of cracking and its growth through the entire laminate, providing a complete view of the damage evolution until the final failure of the composite plate is reached. However, the Hashin-based method only predicts the first ply failure and damage propagation but no crack formation is allowed. Resulting the XFEM a much more powerful and accurate method for the study of the fracture propagation in composite materials. However, thanks to Hashin-based method it is possible to obtain a good first approach that allows to study the laminate behavior when it is subjected to a mechanical action. When comparing XFEM and Hashin-based method results, they are in good agreement until the onset of the failure in the first damaged ply, differing the curves above this point. These differences are greater in the "Reference case" and "Case II" than in the "Case I" and "Case III". The laminates dominated by the 0º plies ("Case I" and "Case III") show that the failure of the first damaged ply will take place later and it will be more progressive and slow, so the force-displacement curves for the Hashin-based analyses will be more linear and they will match better with XFEM analyses.

Regarding to the mechanical properties of the different analyzed plates, it is possible to observe that "Case I" and "Case III" are the laminates that present the best strength values. These two configurations present the maximum number of 0º plies of all the four studied cases, which provide the laminate a greater resistance under tensile loading. The same occurs for the stiffness, due to the 0º direction is the direction of application of the imposed stretching displacements (tensile loading). Regarding "Reference Case" and "Case II", most of the layers are 90º oriented, so they have a low resistance when a tensile load is applied. Therefore, those laminates corresponding to the "Reference case" and "Case II" are weaker than the laminated plates in "Case I" and "Case III". Likewise, the hole radius has also a remarkable importance in the laminate mechanical properties, being able to observe a stiffness reduction as the hole radius increases. The plates with smaller holes are stiffer, experiencing higher stresses for the same applied strain, which leads to an earlier failure.

When comparing "Reference case" and "Case II" and in spite of the fact that both cases present the same number of 0º and 90º plies, it can be appreciated that "Case II" presents better values of strength than the "Reference case". The three 0º plies stacked together in the midline zone of the laminate (Case II) seems to favor the strength of the laminate. Conversely, the same three plies stacked separately lead to lower strength of the laminated plate because they are connected through 90º layers that weaken the resistance of the group. The stiffness is very similar but the strength profit is better using $[90_8, 0, 0, 0, 90_8]$ rather than $[0, 90_8, 0, 90_8, 0]$. However, when comparing "Case I" and "Case III", it can be observed that the large number of 0º plies being placed together cause that the position of the only three 90º plies has not a decisive impact in the results.

Regarding the computational efficiency of both methods, the analyses carried out with XFEM took twice the amount of time than the analyses done with Hashin-based method. This is largely due to the high difference in the number of elements and variables used in XFEM (11420 elements and 77526 variables) and in Hashin-based method (869 elements and 4316 variables).

6.2 Future developments

Despite all the work that has been done in this thesis, there is still a number of tasks that worth being further studied. These include:

- Study of plates without holes but including pre-cracks. Since the numerical test cases done here only consider undamaged plates with holes, this study could be carried out in order to simulate material/manufacturing defects.
- Study of plates with plies having fibre orientations other than 0º and 90º (e.g. 45º or other). This will be an easy task because Abaqus can include any fibre orientation straightforwardly.
- Use of Hashin's criterion with mode-independent fracture energies. These values exist in the literature for some materials. Otherwise, experimental test should be performed to extract these values and include them in the numerical model.
- Application of both XFEM and Hashin-based method to the study of more complex geometries related with components used in the aircrafts (e.g., stiffened skins and fuselages), as well as the analysis of different fiber reinforced composite materials (e.g. carbon fibers) more used in the aviation industry.
- Use of optimization methods to maximize the strength of composite laminated plates through XFEM and Hashin-based analyses, for different layer configurations and fibre orientations.

Finally, it would also be interesting to be able to find techniques to reduce the computational time when carrying out the analyses with the finite element software.

Bibliography

[1] P. L. Jakab, “Wood to Metal: The Structural Origins of the Modern Airplane”, Journal of Aircraft, 36, No. 6, (1999).

[2] US Air Force (USAF) F-117A Nighthawk Stealth Fighter aircraft, (Last updated: 2014). URL: http://www.defenselink.mil/

[3] USAF/Judson Brohmer, Lockheed SR-71 Blackbird, (Last updated: February 6, 2002). URL: http://www.dfrc.nasa.gov/Gallery/Photo/SR-71/HTML/EC94-42883-4.html

[4] Failure in De Havilland Comet, (Last updated: May 5, 2012). URL: http://www.extremetech.com/wp-content/uploads/2012/05/Screen-Shot-2012-05-25-at-9.58.10-AM.png

[5] NTSB, Boeing 737-297 Aloha Airlines, (Last updated: January 29, 2015). URL: http://aviation-safety.net/photos/displayphoto.php?id=19880428-0&vnr=2&kind=C

[6] A-310 rudder separation, (Last updated: October 21, 2011). URL: http://www.skybrary.aero/index.php/A310,_en-route,_Florida_Keys_USA,_2005_(AW_LOC)

[7] L. Ilcewicz, Montana State University Seminar, FAA documentation, (Last updated: October 11, 2009). URL: http://www.coe.montana.edu/me/faculty/cairns/Composites/11-10-09li.pdf

[8] Advisory circular, FAA, Subject “COMPOSITE AIRCRAFT STRUCTURE”, Initiated by: AIR-100. FAA, (Last updated: August 9, 2009). URL: http://www.faa.gov/documentLibrary/media/Advisory_Circular/AC20-107B.pdf

[9] J. H. Heida, D. J. Platenkamp, “In-service Inspection Guidelines for Composite Aerospace Structures”, Aerospace Vehicles, National Aerospace Laboratory NLR, Marknesse, The Netherlands, 18th World Conference on Nondestructive Testing, Durban, South Africa, (2012).

[10] Boeing 787. URL: http://modernairliners.com/Boeing787_files/image342.gif

[11] FAA documentation, Advanced Composite materials. URL:https://www.faa.gov/regulations_policies/handbooks_manuals/aircraft/amt_airframe_handbook/media/ama_Ch07.pdf

[12] A. Fernandez, A. Guemes, J. M. Menéndez, J. Mª Pintado, “Materiales Compuestos (CTA-VA)”, Escuela de Ingeniería aeronáutica y del Espacio, Universidad Politécnica de Madrid, Madrid, Spain (2013).

[13] F. Paris, "A study of failure criteria of fibrous composite materials", NASA/CR- 2001-210661, (2001).

[14] A.S Tetelman, “Fracture processes in fiber composite materials, in Composite materials: Testing and design”, American society for testing and materials, 473-502, New Orleans, Louisiana, (1969).

[15] S. W. Tsai, “Strength Characteristics of Composite Materials”, NASA CR-224, (1965).

[16] S. W. Tsai and E. M. Wu, “A general theory of strength for anisotropic materials”, Journal of Composite Materials, 5, 58-80, (1971).

[17] Z. Hashin, “Failure criteria for unidirectional fiber composites”, Journal of Applied Mechanics, 47, 329-334, (1980).

[18] Z. Hashin and A. Rotem, "A fatigue failure criterion for fiber reinforced materials", Journal of Composite Materials, 7, 7448-7464, (1973).

[19] F. Cañas, J. Marín, J. C. Barroso, A. Paris, “Introducción al análisis y diseño con materiales compuestos. Sección de publicaciones”, Universidad de Sevilla, ETS Ingenieros, Ed., Sevilla, Spain (2008).

[20] R. M. Jones, “Mechanics of Composite Materials”, Mc Graw-Hill, New York, USA, (1975).

[21] H. M. Deuschle, “3D Failure Analysis of UD Fibre Reinforced Composites: Puck’s.Theory within FEA”, (PhD thesis,) Universität Stuttgart, (2010).

[22] M. M. Moure, S. Sanchez-Saez, E. Barbero, E. J. Barbero, “Analysis of damage localization in composite laminates using a discrete damage model”, Composites: Part B, 66, 224-232, (2014).

[23] P. Liu, L. Xing, J. Zheng, “Failure analysis of carbon fiber/epoxy composite cylindrical laminates using explicit finite element method”, Composites Part B: Engineering, 56, 54-61, (2014).

[24] E. J. Barbero, G. Sgambitterra, A. Adumitroaie, X. Martinez, “A discrete constitutive model for transverse and shear damage of symmetric laminates with arbitrary stacking sequence”, Composite Structures, 93, 1021-1030, (2011).

[25] A. A. Griffith, “The Phenomena of Rupture and Flow in solids”, Philosophical transactions of the Royal Society, Vol. 221A, 163-198, (1920).

[26] G. R Irwin, “Fracture, in handbuch der physic”, Vol. V, Springer, New York, (1958).

[27] H. T. Corten, “Micromechanics and fracture behavior of composites, in modern composite materials”, Addisoon-Wesley, 27-105, New York, (1967).

[28] E. J. Barbero, “Introduction to composite materials design”, 2nd ed. Philadelphia, PA: CRC PRESS, (2011).

[29] E. J. Barbero, “Finite element analysis of composite materials”, CRC Press, Boca Raton, FL, (2007).

[30] E. J. Barbero, D. H. Cortes, ”A mechanistic model for transverse damage initiation, evolution, and stiffness reduction in laminated composites”, Composites: Part B, 41,124-132, (2010).

[31] T. Belytschko, T. Black, “Elastic crack growth in finite elements with minimal remeshing”, International Journal of Numerical Methods in Engineering, 45, 601-620, (1999).

[32] J. M. Melenk, I. Babuska, “The partition of unity finite element method: basic theory and applications”, Computational Methods Applied in Mechanics and Engineering, 139, 289-314, (1996).

[33] D. Motamedi, S. Mohammadi, “Fracture analysis of composites by time independent moving-crack orthotropic XFEM”, International Journal of Mechanical Sciences, 54, 20-37, (2012).

[34] Z. Z. Du, “eXtended Finite Element Method (XFEM) in Abaqus. Dassault Systémes”.

[35] Simulia, “Abaqus/CAE”, version 6.10, 2010. User’s manual.

[36] Z. M. Huang,”Failure analysis of laminated structures by FEM based on nonlinear constitutive relationship”, Composites Structures, 77, No. 3, 270-279, (2007).

[37] Z. M. Huang, “Simulation of the mechanical properties of fibrous composites by the bridging micromechanics model”, Composites Part A: Applied Science and Manufacturing, 32, 143-172, (2001).

[38] X. Chen, Z. Li, H. Wang, “Progressive failure analysis of an open-hole composite laminate by using the s-version finite-element method”, Mechanics of composite materials, 50, No. 3, (2014).

[39] E. J. Barbero, F. A. Cosso, X. Martinez, “Identification of fracture toughness for discrete damage mechanics analysis of glass-epoxy laminates”, Applied Composite Materials , 1-18, (2013).

[40] E. J. Barbero, F. A. Cosso, R. Roman, T. L. Weadon, “ Determination of material parameters for Abaqus progressive damage analysis of E-glass epoxy laminates”, Composites Part B, 46, 211–220, (2013).

[41] A. M. Girao Coelho, J. T. Mottram, K. A. Harries, ”Finite element guidelines for simulation of fibre-tension dominated failures in composite materials validated by case studies”, Composite Structures 126, 299-313, (2015).